University of Alberta

Morphology Control and Localized Surface Plasmon Resonance in Glancing Angle Deposited Films

by

Douglas Arthur Gish

A thesis submitted to the Faculty of Graduate Studies and Research
in partial fulfillment of the requirements for the degree of

Master of Science
in
Microsystems and Nanodevices

Department of Electrical and Computer Engineering

Fall 2010
Edmonton, Alberta

Examining Committee

Michael Brett, Electrical and Computer Engineering

Jeremy Sit, Electrical and Computer Engineering

Mark McDermott, Chemistry

To my family.

ABSTRACT

This research investigates an extension of the glancing angle deposition (GLAD) technique and a biosensing application of films produced by GLAD. The extension to GLAD, called phi-sweep (PS), improves column isolation compared to films grown by traditional GLAD (TG) as well as modifies the column tilt angle, β, of the slanted columns according to $\tan(\beta_{PS}) = \tan(\beta_{TG})\cos(\gamma)$, where γ is the sweep angle. The biosensing application makes use of localized surface plasmon resonance in noble metal GLAD films functionalized with rabbit immunoglobulin G (rIgG) to detect binding of anti-rabbit immunoglobulin G (anti-rIgG) to the films' surface. The extinction peak red-shifts a distance dependent on the concentration of anti-rIgG solution in a manner described by the Langmuir isotherm with a saturation value, $\Delta\lambda_{max}$, of 29.4 ± 0.7 nm and a surface confined thermodynamic binding constant, K_a, of $(2.7 \pm 0.3) \times 10^6$ M^{-1}.

ACKNOWLEDGEMENTS

First I would like to thank my family. My loving wife Treena has been very patient, supportive and encouraging. Without her I would never have completed this thesis. My little daughter Anna has helped me as well by bringing many smiles to my face. I would also like to thank my parents. From a young age they instilled in me a drive to always work hard and do my best.

It has been a pleasure working with my supervisor, Dr. Brett. His feedback has been immensely helpful in the completion of this research. His patience and encouragement have been greatly appreciated.

I'd also like to thank all of my fellow researchers in the GLAD group. They are a wonderful, fun group of people. A special thank you goes to Mark Summers, who in addition to being a great friend, spent countless hours taking SEM images for me. Also, my thesis looked much better after applying the LaTeX style he created and graciously allowed me to use. Thank you Jason Sorge, Andy van Popta, Matthew Hawkeye, Louis Bezuidenhout, Josh LaForge, Mike Taschuk, Jeremy Sit, Mike Fleischauer, Nick Wakefield, Sumudu Fernando, Graeme Dice, Jonathan Kwan, Katie Krause, Martin Kupsta, Jaron van Dijken, John Steele, James Gospodyn, Shufen Tsoi, Anastasia Elias, Ken Harris, Scott Kennedy, Martin Jensen, Peter Hrudey, Steven Jim, Zhifeng Huang, Joshua Krabbe, and Michael Thomas. I've made many friends in the GLAD group with whom I hope to stay in touch.

Finally, I would like to acknowledge funding from the Natural Sciences and Engineer-

ing Research Council of Canada, the Alberta Ingenuity Fund, the Informatics Circle of Research Excellence, and the University of Alberta. Without their support, this research would not have been possible.

CONTENTS

1 Introduction 1

1.1 Phi-Sweep . . . 3

1.2 LSPR Biosensing . . . 3

2 Glancing Angle Deposition 4

2.1 Thin Films . . . 4

2.2 Physical Vapour Deposition . . . 4

2.3 Oblique Deposition . . . 5

2.4 Glancing Angle Deposition . . . 7

2.4.1 Apparatus . . . 8

2.4.2 Sample Film Morphologies . . . 9

2.4.3 Applications of GLAD . . . 9

3 Phi-Sweep 12

3.1 Background . . . 12

3.2 Experimental Procedure . . . 17

3.3 Results and Discussion . . . 18

3.3.1 Phi-Sweep Slanted Post Tilt Angle Derivation . . . 18

3.3.2 Measured Tilt Angles of Si and TiO_2 Slanted Posts on Patterned Substrates . . . 19

3.4 Conclusion 26

4 LSPR in GLAD Films **27**

4.1 Introduction 27

4.2 Background and Theory 27

4.3 Sphere-like Particle Films 32

4.4 Slanted Post Films 39

4.5 Phi-Sweep Films 47

4.6 Ageing Effects 50

5 LSPR Biosensing with GLAD Films **53**

5.1 Introduction 53

5.2 Experimental Procedure 53

5.2.1 Extinction Measurements 54

5.2.2 Biosensor Preparation and Testing 55

5.3 Results and Discussion 57

5.4 Conclusion 64

6 Conclusion **65**

6.1 Summary of Research Results 65

6.2 Suggested Future Work 66

6.3 Final Remarks 67

References **68**

LIST OF TABLES

3.1 Measured and predicted column tilt angles, β, of Si slanted post films deposited with sweep angles, γ, of 0°, 30°, and 45°. The column tilt angles were independently measured on the 100, 200, and 300 nm periodicity patterned substrates. 22

3.2 Measured and predicted column tilt angles, β, of TiO_2 slanted post films deposited with sweep angles, γ, of 0° and 45°. The column tilt angles were independently measured on the 100, 200, and 300 nm periodicity patterned substrates. 23

LIST OF FIGURES

2.1 Schematic of a) nucleation and self-shadowing effect, and b) growth of isolated columns. 6

2.2 A schematic of the GLAD apparatus. 8

2.3 Examples of thin films with various morphologies created by the GLAD process. 10

3.1 Schematic of anisotropic broadening of GLAD columns. The self-shadowing limits broadening in the x-direction, but not in the y-direction. 13

3.2 Schematic of a) the traditional GLAD technique and b) the phi-sweep technique. The sweep angle is given by γ. 14

3.3 Schematic of a) a traditional GLAD column and b) a column produced by the phi-sweep technique. β_{TG} and β_{PS} are the column tilt angles of the traditional GLAD column and the phi-sweep column, respectively, and q is the sweep pitch. 15

3.4 SEM images of the a) top and b) side of a silicon film grown using phi-sweep. The film was grown with a deposition angle of 82°, a sweep pitch of 45 nm, and a sweep angle of 45°. 16

3.5 Top down SEM images of the **a)** 100, **b)** 200, and **c)** 300 nm periodicity patterned substrates. 17

3.6 Phi-sweep β derivation model. 20

3.7 Column tilt angle, β, as a function of deposition angle, α, for various sweep angles, γ. 20

3.8 Side view SEM images of the Si slanted post films fabricated using **a)**, **b)**, **c)** traditional GLAD, **d)**, **e)**, **f)** phi-sweep with a sweep angle of 30°, and **g)**, **h)**, **i)** phi-sweep with a sweep angle of 45° on 100, 200, and 300 nm periodicity substrates, respectively. 22

3.9 Top view SEM images of the Si slanted post films fabricated using **a)**, **b)**, **c)** traditional GLAD and **d)**, **e)**, **f)** phi-sweep with a sweep angle of 30° on 100, 200, and 300 nm periodicity substrates, respectively. 24

3.10 Oblique view SEM images taken at 45° from the substrate normal of the TiO_2 slanted post films fabricated using **a)**, **b)**, **c)** traditional GLAD and **d)**, **e)**, **f)** phi-sweep with a sweep angle of 45° on 100, 200, and 300 nm periodicity substrates, respectively. 25

4.1 Schematic of localized surface plasmon oscillation for a metal sphere. The conduction electron charge cloud is displaced due to the incident electric field. 29

4.2 Calculated extinction spectra for samples of 50 nm radius silver particles with an area fraction of 0.5 are shown in a) using media of various index of refraction with χ = 2 and b) using different values for χ in an vacuum medium. 30

4.3 Calculated extinction spectra for samples of 100 nm radius gold particles with an area fraction of 0.5 are shown in a) using media of various index of refraction with χ = 17 and b) using different values for χ in an vacuum medium. 31

4.4 SEM images of four silver samples grown using constant phi-rotation at deposition angles of a) 79°, b) 81°, c) 83°, and d) 85°. 34

4.5 Extinction spectra of four silver samples grown using constant phi-rotation at different deposition angles. 35

4.6 Side-view SEM image of a 177 nm thick silver film grown using constant phi-rotation. 36

4.7 SEM images of four silver samples grown using constant phi-rotation with thicknesses of a) 4 nm, b) 14 nm, c) 150 nm, and d) 177 nm. 37

4.8 Extinction spectra of silver samples grown using constant phi-rotation with different thicknesses. 38

4.9 SEM images of gold slanted post films. The average post length for each sample is a) 62 nm, b) 98 nm, c) 111 nm, d) 138 nm, e) 174 nm, and f) 198 nm. 40

4.10 Side-view SEM image of 198 nm average length gold slanted post sample. 41

4.11 Length of gold slanted posts for samples grown at different distances from the source material. 41

4.12 Longitudinal extinction spectra of gold slanted post films of different average lengths in a) air and b) water. 43

4.13 Transverse extinction spectra of gold slanted post films of different average lengths in a) air and b) water. 44

4.14 Localized surface plasmon resonant wavelength of gold slanted post samples with different average post lengths for both the transverse and longitudinal polarizations. 45

4.15 Refractive index sensitivity of gold slanted post samples of different average lengths. The sensitivity is the wavelength shift in nanometres per refractive index unit (RIU). 46

4.16 Scanning electron microscopy images of a 50 nm thick gold slanted post film grown using (a) traditional GLAD, and (b) phi-sweep. 48

4.17 Extinction spectra of both a 50 nm thick traditional GLAD slanted post film and a 50 nm thick phi-sweep film for both the a) transverse and b) longitudinal polarizations. 49

4.18 a) SEM image of a 20 nm thick spherical gold film and b) extinction spectra of the film over a two week period. Time shown is time elapsed from removal from the deposition chamber. 51

4.19 Change in a) peak extinction and b) peak wavelength of a 20 nm thick spherical gold film over a two week period. Time shown is time elapsed from removal from the deposition chamber. The curves are a guide to the eye. 52

5.1 Noise equivalent extinction for a typical sample. One of the extinction spectra used to calculate the noise equivalent extinction is also shown. . 56

5.2 Scanning electron microscopy images of (a) the top surface, and (b) the cross-section of the Ag nanoparticle film on a fused silica substrate. . . 58

5.3 (a) Extinction spectra in air of an as deposited film, and after being immersed in solvents for various time periods. (b) Extinction spectra in air before solvent measurements, in solvents of varying index of refraction, and in air again after the solvent measurements. The refractive index of each solvent is 1.33, 1.38, and 1.45 for water, 2-propanol, and chloroform, respectively. 60

5.4 The initial extinction curve before sample functionalization, and extinction curves after the 11-AUT and rIgG functionalization steps. 61

5.5 (a) Extinction spectrum of rIgG functionalized sample, and a selection of the extinction spectra after exposure to solutions of varying concentrations of anti-rIgG. (b) Peak LSPR extinction wavelength shift as a function of anti-rIgG concentration. The curve is a fit to the Langmuir isotherm given in Eq. 5.2. The error bars are estimates of the uncertainty in the wavelength shifts. 63

5.6 Extinction spectrum of rIgG functionalized sample, and spectra after incubation in 1 mM PBS, 1.06 μM anti-gIgG, and 1.06 μM anti-rIgG. . . 64

1 INTRODUCTION

Thin film technology has revolutionized modern life. From electronic semiconductor technology and optical filters to protective and aesthetic coatings, we benefit from the use of thin films daily. The continual improvement of thin film technology and engineered materials relies on the development of increasingly sophisticated fabrication techniques. Recently, much of this development has been directed toward the fabrication of nanostructured thin films. These are films which incorporate morphology with features at size scales of typically 1 - 100 nm. There are several methods of nanostructure fabrication. These are generally categorized into either top-down or bottom-up approaches.

Top-down techniques include electron beam lithography, where focused beams of electrons are directed at an electron beam resist. Different areas of the resist become soluble or insoluble depending on whether they have been exposed to the electron beam. Electron beam lithography has been shown to be capable of fabricating structures with a resolution smaller than 10 nm [1]. Other top-down techniques include dip-pen lithography, which uses the tip of a cantilever scanning across a surface to deliver some form of molecular or nanoparticle "ink". This ink normally chemically binds to the surface and forms stable patterns as small as 30 nm in width [2]. A somewhat related technique is nanoimprint lithography, in which a patterned mold, or master, is coated with material and "stamped" onto a surface, leaving behind a copy of the pattern [3]. An alternate method of nanoimprint lithography is to physically deform the surface of some soft material such as a polymer with the patterned mold. Some advantages of the top-down approaches are that the degree of control over the placement and morphology of the resulting structures is relatively high compared to structures produced by bottom-up approaches. However, the top-down methods are usually more expensive and time-consuming.

Bottom-up approaches typically exploit special effects that occur in nature to have a material automatically organize itself into nanostructures. There are numerous nanostructures and molecules with interesting properties that can be synthesized through chemical

means, such as single- or multi-walled carbon nanotubes. Carbon nanotubes have been reported to have mechanical properties exceeding those of any other known material [4]. Another common example of the bottom-up approach is molecular self-assembly. Molecular self-assembly makes use of certain molecules that minimize their potential energy when they arrange themselves in some ordered fashion. For example, this can be used to form self-assembled monolayers of molecules, such as alkanethiols, onto a surface [5]. Periodic nanostructures can be formed on a surface using the self-assembly of block copolymers [6]. Molecular self-assembly can also be used to aid in the assembly of nanostructures produced by other techniques, such as tiny hexagonal plates, into larger arrays or sheets [7]. In addition to molecular self-assembly, certain nanostructures, such as nanospheres, will self-assemble into organized arrays. Nanosphere lithography uses self-assembled hexagonally closed packed arrays of nanospheres on a substrate as shadow-masks for subsequent deposition of material through the mask [8]. After removal of the nanospheres, an array of triangular nanoparticles of the deposited material is left on the substrate. Another technique is the electrochemical etching of silicon to create nanoporous silicon films [9]. The pores are thought to form due to the formation of space charge regions on the doped silicon surface [10]. Although current electronic chip fabrication makes use of the top-down approach almost exclusively, many researchers believe that bottom-up approaches, such as molecular self assembly, will soon be used in conjunction with standard techniques due to its low cost and convenience [7].

One bottom-up technique that has opened up a new area of research in the thin film community is glancing angle deposition (GLAD). Using this technique, one can fabricate porous, columnar thin films comprised of many individual columns of material, the morphology of which can be controlled at nanoscale dimensions. Glancing angle deposition is a flexible technology which is able to work with a wide variety of different materials, and the ability to control the morphology of thin films at the nanoscale allows for a material's physical properties to be tailored for a specific use. This has led to GLAD films being developed for a wide variety of applications, including sensors, optical filters, catalysts, and solar cells.

GLAD technology has been continually improved and refined for over a decade now, but there are still many opportunities to advance the technology. One problem that inhibits the design of a material's properties using the traditional GLAD technique is the limited control the technology provides over the cross-sectional morphology of the

individual columns in a film. Due to competitive growth of the columns during the film fabrication process, some columns increase in diameter or "broaden" as they grow, while other columns decrease in diameter and their growth can eventually get extinguished. In addition, the columns commonly develop a highly elliptical cross-section due to an effect called column "fanning", which can often be undesirable.

1.1 Phi-Sweep

Fortunately, the broadening and fanning effects can be suppressed using an extension of the GLAD technique called phi-sweep. Phi-sweep was originally developed by Jensen and Brett to improve the fabrication of photonic bandgap materials based on GLAD films, and was shown to dramatically reduce column broadening. This thesis expands on that initial research by exploring not only the impact of the phi-sweep technique on cross-sectional column morphology, but other aspects of the film's morphology as well. Specifically it clearly shows that phi-sweep reduces column fanning, and provides a model describing how column tilt angle is dependent on phi-sweep parameters. The model's validity is tested and proven experimentally.

1.2 LSPR Biosensing

There has been substantial research towards using GLAD films for sensing. For instance, metal oxide films seem to be particularly well suited to high speed humidity sensing, and there are several reports regarding this subject. One area that is yet to be fully explored is sensing biomolecules using GLAD films. It is well known in the literature that metal nanoparticles can have unique optical properties due to localized surface plasmon resonance (LSPR). These properties are highly dependent on a nanoparticle's size and shape, as well as conditions at the particle's surface. The latter dependence can be exploited to detect the binding of molecules to metal particles. This thesis explores the use of gold and silver GLAD films towards biomolecule sensing using LSPR. The phi-sweep technique was used in an attempt to improve the morphology of these films. However, phi-sweep provided no significant benefit for this particular application.

2 GLANCING ANGLE DEPOSITION

Glancing angle deposition (GLAD) is a thin film deposition technique, and an extension of physical vapour deposition that provides enhanced control over thin film morphology than is possible using traditional techniques. The GLAD process takes advantage of the inherent columnar nature of thin films, while exploiting the self-shadowing effect that occurs at oblique deposition angles. The combination of oblique deposition with precision substrate rotation has allowed for the growth of highly porous thin films with complex morphology on nanometre size scales to be tailored in a single-step deposition process.

2.1 Thin Films

Thin films are used in a wide variety of applications that we encounter in daily life. Modern electronic devices such as microprocessors and flat panel displays would not be possible without thin film deposition and processing technology. Optical coatings, such as anti-reflective coatings, are also composed of thin films. Another example is protective coatings with high hardness on cutting tools that increase the tools' lifetime. A thin film is usually classified as a thin layer of material ranging between a few angstroms to several micrometres. Thin films are typically applied to the surface of some other material, known as the substrate. The act of applying a thin film to a substrate is called thin film deposition. There are two main categories of deposition techniques: physical deposition and chemical deposition. Due to the need for a high degree of collimation of an incoming vapour flux, the GLAD process requires that a physical vapour deposition technique is used.

2.2 Physical Vapour Deposition

Physical vapour deposition (PVD) involves the adsorption of material from a gaseous state onto a solid substrate. The main types of PVD include evaporation, sputtering, and laser

ablation. There are two main types of evaporation: thermal and electron beam (e-beam). In either case for evaporation, the source material is heated to a high enough vapour pressure that it begins to evaporate at a sufficiently high rate. In thermal evaporation this is accomplished by electrically resistive heating, while during e-beam evaporation the material is heated via electron bombardment. During sputtering, vapour from a target material is produced by ion bombardment in a plasma. Finally, laser ablation involves vapourization of material by a high powered pulsed laser.

Each of these PVD techniques allows for a different set of parameters and conditions to be controlled during thin film growth. Therefore, one technique may be more suitable than another for a specific application. An important consideration for the GLAD method is the degree of collimation of the vapour flux impinging on the substrate, as well as the kinetic energy of the adsorbed atoms. Another consideration is how amenable a particular material is to being deposited by a certain technique. Due to the high degree of vapour flux collimation and the wide variety of compatible materials, the most common technique used for the GLAD process is electron beam evaporation. However, it has also been demonstrated using sputtering [11] and pulsed laser ablation [12].

2.3 Oblique Deposition

In a traditional PVD process, the substrate is typically held such that the incoming vapour flux arrives normal to the substrate surface. However, the effects of holding the substrate at an oblique angle from the incoming vapour flux have been studied for more than 100 years. Early researchers discovered that thin films grown using oblique deposition had interesting properties such as dichroism, birefringence, and anisotropic resistivity [13, 14, 15, 16]. In the 1950's and 60's, obliquely deposited thin films with magnetic anisotropy were reported [17, 18, 19]. The anisotropic properties were attributed to grain elongation due to atomic-scale shadowing, or "self-shadowing" during the deposition process [20, 21].

When a molecule adsorbs onto the substrate, it can migrate a short distance due to surface diffusion before settling in an energetically favourable position. This causes the particles to clump together to form small mounds, or nuclei, on the substrate surface. The self-shadowing effect occurs when incident vapour particles are blocked from reaching an area of the substrate by a nucleus, as shown in Figure 2.1(a). These shadowed areas become voids in the film. Whether or not a particular particle is blocked in this way

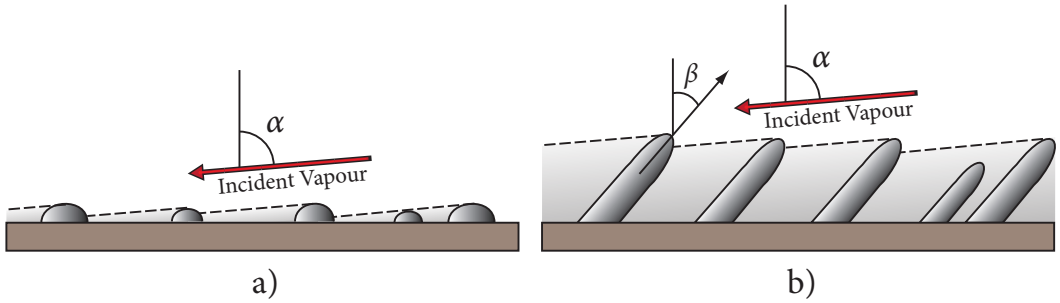

Figure 2.1: Schematic of a) nucleation and self-shadowing effect, and b) growth of isolated columns.

depends strongly on its trajectory. If a particle arrives at a highly glancing angle, it has a much greater chance of being blocked. Therefore, the amount of shadowing is heavily dependent on the deposition angle, α, and the degree of collimation of the incident flux. When the deposition angle is sufficiently high, and the vapour flux sufficiently collimated, the size and amount of voids increases to the point at which the film is composed of isolated columns in a void matrix. This is shown in Figure 2.1(b). The deposition angle at which this occurs is typically greater than approximately 70°. The columns tilt towards the source at an angle, β, with respect to the substrate normal. The relationship between deposition angle and tilt angle can be described by Eq. 2.1, which was geometrically derived by Tait et al. in 1993[22].

$$\beta = \alpha - \arcsin\left(\frac{1-\cos\alpha}{2}\right) \tag{2.1}$$

Tait also described the change in film density, ρ, as a function of deposition angle, as shown in Eq. 2.2.

$$\rho = \frac{2}{1+\frac{1}{\cos\alpha}} \tag{2.2}$$

This shows that the density decreases as α increases, as expected, since there are more voids in the film with increasing deposition angle due to the shadowing effect.

Since it is often desirable to achieve a film with well isolated columns, it is clear that a highly collimated vapour flux is important. To improve the collimation of the flux, several techniques can be used. One technique is increasing the throw distance between the source and the substrate to narrow the cone of accepted angles that are intercepted

by the substrate. The use of this technique is limited by the size of the vacuum chamber, and has the side effect of an increased amount of wasted material that is deposited on the chamber walls. The acceptance cone can also be narrowed by reducing the size of the source. Introducing a physical collimator consisting of a series of collimating channels between the source and the substrate can also reduce the angular spread of particles that reach the substrate [23]. Finally, the chamber pressure can be lowered to reduce the number of scattering events and increase the mean free path of the particles.

The columns in a film grown by oblique deposition are normally distributed randomly across the substrate. However, the position of the columns can be controlled by pre-patterning the substrate topography with small hills or "seeds" in positions matching the desired placement of the columns. This imposes shadowing conditions on the substrate which cause the incoming vapour flux to preferentially land on top of the seeds, rather than between them. By tailoring the substrate topography so that the planar filling fraction of the seeds is roughly equal to the equilibrium volumetric filling fraction of the film, growth of a single isolated column per seed can be achieved. Pre-patterned substrates are commonly used to create films where the columns are arranged in periodic arrays [24, 25, 26]. Methods of creating pre-patterned substrates include electron-beam lithography [26], laser direct-write lithography [26], self-assembly of silica spheres [27] and photolithography [26, 28].

2.4 Glancing Angle Deposition

Glancing angle deposition extends oblique deposition by adding computer controlled substrate rotation about the substrate normal. This allows for thin films with a myriad of complex morphologies to be engineered. Apart from an early experiment in 1959 [29], the combination of oblique deposition and substrate rotation was not studied until 1996 by Robbie and Brett [30, 31, 32]. They realized that by rotating the substrate, the morphology of obliquely deposited films was no longer restricted to simple slanted columns that tilted towards the source. Substrate rotation causes the effective position of the source to change with respect to the substrate, and subsequent column growth will track the new source position. Controlling the substrate rotation controls the film morphology. The rotation about the substrate normal is described by the angle ϕ.

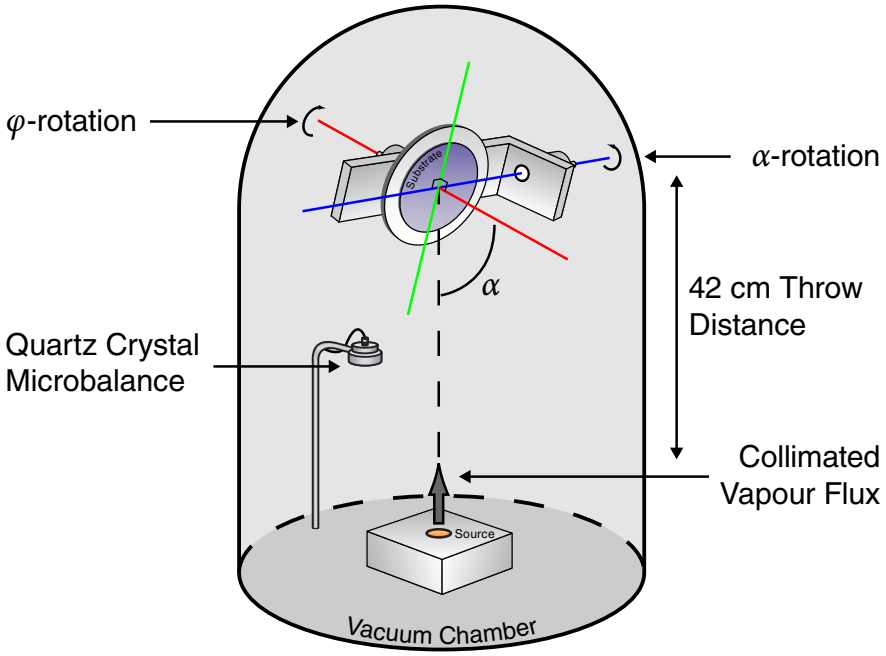

Figure 2.2: A schematic of the GLAD apparatus.

2.4.1 Apparatus

A schematic of the apparatus used for the GLAD process is shown in Figure 2.2. An e-beam evaporator is situated at the base a vacuum chamber. Electrons are thermionically emitted from a filament and accelerated by a high voltage of typically 6-9 kV. These electrons are directed to the source by a magnetic field, which heats the source material. The substrate is held 42 cm above the source, and its position is controlled by two motors. These motors are able to rotate the substrate about two axes: the α-axis in the plane of the substrate, and the ϕ-axis normal to the substrate. Rotating about the α-axis changes the angle at which the incident flux arrives at the substrate. This affects the density of the thin film, as well as the tilt angle of the columns in the film. Rotation about the ϕ-axis controls the chiral structure of the GLAD film. A quartz crystal microbalance monitors the deposition rate, which allows the computer controlled motors to move precisely and compensate their rotation speed if the rate changes. The vacuum chamber is typically held at pressures in the $\sim 10^{-8}$–10^{-5} Torr range during a deposition.

2.4.2 Sample Film Morphologies

Some of the possible thin film morphologies created via the GLAD process are the following:

- Slanted Columns: This is the basic morphology that is produced using standard oblique deposition, which can be seen in Fig. 2.3a.
- Helices: By continuously rotating the substrate during the deposition, the column growth direction also continuously rotates, resulting in helical shape. The speed of rotation controls the radius of the helix. An image of a helical film is shown in Fig. 2.3b.
- Vertical Columns: These are also grown using continuous rotation, but at a higher rotation speed. This causes the helical pitch to become so small that the helix degenerates into a vertical post structure, shown in Fig. 2.3c.
- Zigzags: By growing a series of slanted column segments separated by abrupt 180° turns, a zigzag structure can be grown as seen in Fig. 2.3d.
- Polygonal Helices: If instead of abrupt 180° turns between vertical column segments, some other angle is used, polygonal helix films can be engineered. This is shown in Fig. 2.3e, where abrupt 90° turns result in a square helix film. Figure 2.3e is also an example of a film that was grown onto a pre-patterned substrate where the seeds were placed in a tetragonal array.
- High-Low Stack: The deposition angle need not stay constant during the deposition, and can be changed to alter the density of the film, as described by Eq. 2.2. The result of this is shown in Fig. 2.3f, where the substrate is rotated continuously to grow a vertical post film, but the deposition angle is abruptly changed between a high and low value. This creates a periodic stack of high and low density layers.

2.4.3 Applications of GLAD

Since 1996, there has been a lot of study and interest in the unique properties and applications of thin films grown by GLAD. Many of the applications are optical due to the

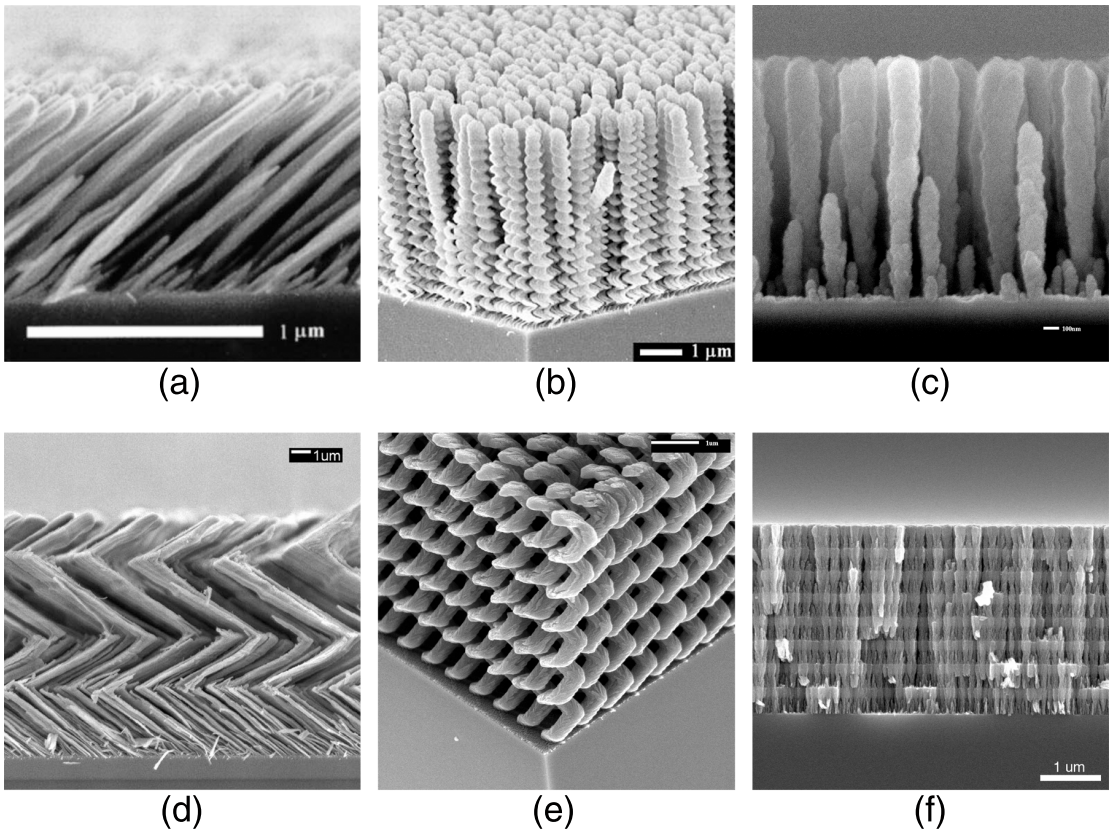

Figure 2.3: Examples of thin films with various morphologies created by the GLAD process. Reproduced with permission from M. Summers [33]. Image a) reprinted with permission from [34]. Copyright 1998, American Vacuum Society. Image b) reprinted by permission from Macmillan Publishers Ltd: Nature[30], copyright 1996. Image e) reprinted with permission from [35].

high degree of control GLAD provides over the morphology of films at the appropriate size scale for optical applications. These include birefringent films [36, 37, 38], narrow bandpass filters [39, 40], anti-reflection coatings [41], polarization selective chiral films [42], and photonic bandgap materials [28, 43, 44, 45]. Many applications exploit the high surface area of GLAD thin films, including catalysis [46, 47], energy applications such as solar cells [48], and sensor applications such as high speed humidity sensing [49, 50, 51]. There have also been many studies on the mechanical properties of helical films as nanosprings [52, 53, 54, 55], as well as the electrical properties of films under load [56]. Most GLAD studies have focused on metals or metal oxides, but recently there has been work done with organic materials as well [57, 58, 59].

3 PHI-SWEEP[1]

3.1 Background

A well-known characteristic of films grown using GLAD is that during film growth the individual columns compete for the incoming vapour flux. This results in the extinction of some of the columns and the broadening of others. Due to the anisotropy of the self-shadowing effect, this broadening is also anisotropic, as shown in Figure 3.1 [61, 62, 63]. The shadowing from nearby columns constrains broadening along the x-axis. However, due to the shadowing direction, broadening is not well constrained along the y-axis. This results in the columns developing a highly elliptical cross-section, with the long axis in the direction perpendicular to the plane of incidence. This effect is sometimes referred to as column "fanning" and is often undesirable.

One application of GLAD for which broadening and fanning are especially detrimental is the fabrication of photonic bandgap crystals. Glancing angle deposition has been shown to be a good method for the fabrication of photonic crystals consisting of a periodic array of square spirals [28]. This structure is based on the family of [001]-diamond:n crystal lattices [64]. The n^{th} nearest neighbour points of the original diamond lattice are connected by the square spiral arms. The square spiral structures that yield the largest band gaps are those where $n = 1$ or $n = 5$. The performance of the photonic crystal is strongly dependent on the quality of the square spiral structure, which is significantly reduced by broadening and fanning effects.

To improve the quality of photonic crystals, an extension of the GLAD process called phi-sweep GLAD has been developed which utilizes advanced substrate motion to provide even greater control over the cross-sectional morphology of columns in nanostructured thin films [65]. In traditional GLAD, the substrate is kept still during the growth of a linear slanted post segment, as shown in Figure 3.2a; whereas, in phi-sweep GLAD, the substrate is swept back and forth around the ϕ-axis, subtending an angle called the sweep angle, γ, from either side of the desired growth direction. After each sweep, the substrate

[1] A version of this chapter has been published in Ref. [60].

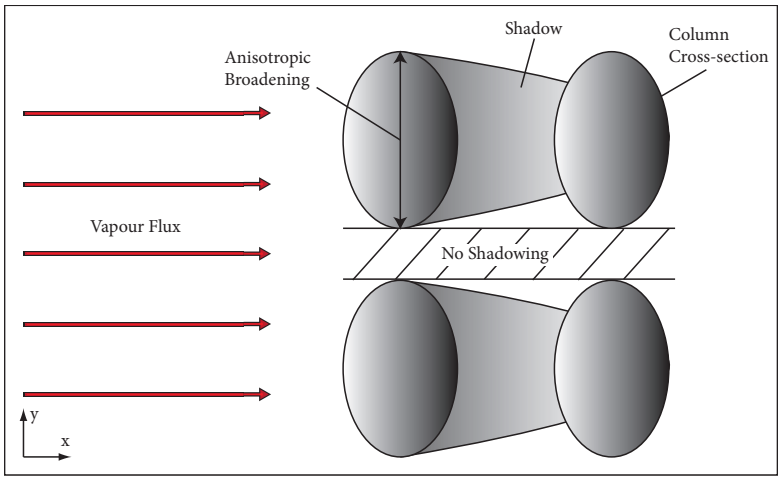

Figure 3.1: Schematic of anisotropic broadening of GLAD columns. The self-shadowing limits broadening in the x-direction, but not in the y-direction.

is held in position until the film has grown a certain thickness called the sweep pitch, q, before sweeping the substrate back in the other direction, as shown in Figure 3.2b. This process breaks the anisotropy in the shadowing conditions and delays the column broadening that begins just after film nucleation. The value of the sweep pitch must be chosen appropriately to maximize the broadening reduction [65]. If the sweep pitch is too large, significant broadening can occur between substrate sweeps, due to the prolonged period of anisotropic shadowing. If the sweep pitch is too small, the rapid alternation of flux arrival will degenerate the growing columns into lumps, as the material quickly accumulates on two sides of the columns. It is thought that the optimum sweep pitch is related to the initial width of the columns that form just after nucleation [65]. A schematic of the resulting column morphology as compared to that of traditional GLAD films is shown in Figure 3.3, and an SEM image of a typical silicon film produced using phi-sweep is shown in Figure 3.4. In the top-down image in Fig. 3.4a, the column cross-sections are quite uniform and show very little column fanning. From the side-view image in Figure 3.4b, it is evident that there is little column broadening over the 2 μm thick film. The periodic rippling seen in the side-view image is caused by the change in growth direction due to the phi-sweep technique.

Jensen and Brett have shown the phi-sweep technique enables columnar architectures of widths as small as 20 nm to be fabricated in a single step process [65]. Changing the parameters of the phi-sweep method, in particular the sweep pitch, allows for control over

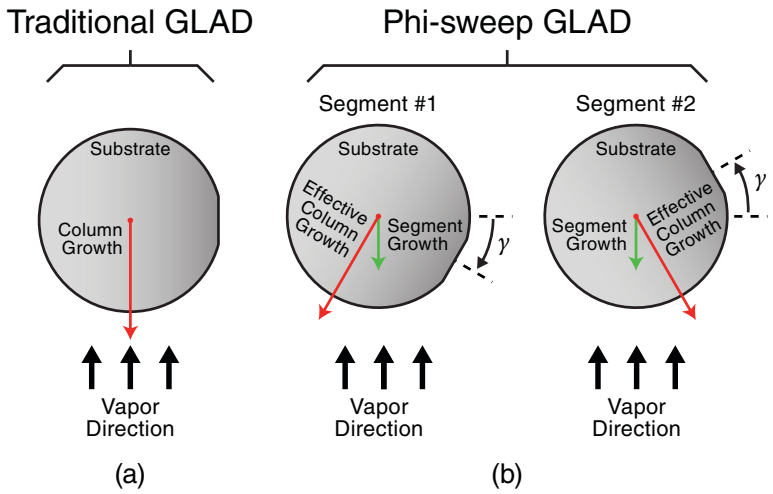

Figure 3.2: Schematic of a) the traditional GLAD technique and b) the phi-sweep technique. The sweep angle is given by γ.

the quantity and size scale of voids in the film independent of the film's density or helical structure. This capability allows for the fabrication of highly porous thin films consisting of fibres much smaller in diameter than those attainable with traditional GLAD. Although phi-sweep films have the same overall density as traditional GLAD films, phi-sweep films can be engineered to have a greater number of smaller pores. Consequently, such films have an estimated one order of magnitude higher surface area than traditional GLAD films, which already have a greatly enhanced surface area compared to conventional thin films [65]. Jensen and Brett have also demonstrated the use of phi-sweep to fabricate photonic crystals in 2005 [43].

The photonic crystal structures have optimal column tilt angles of the square spiral arms which maximize the band gap. For instance, the optimized structure corresponding to [001]-diamond:1 has a column tilt angle of 64° measured from the substrate normal; whereas, the optimal structure corresponding to [001]-diamond:5 requires an angle of 79° [64]. Therefore, it is important to understand how the phi-sweep method affects the column tilt angle. This study investigates the relationship between the phi-sweep parameters and the column tilt angle of the resulting nanostructured thin films. The relationship is derived using geometrical arguments, and observed by measuring the column tilt angle of a series of films consisting of periodic arrays of slanted post structures grown using the phi-sweep method. These results are compared to similar films grown

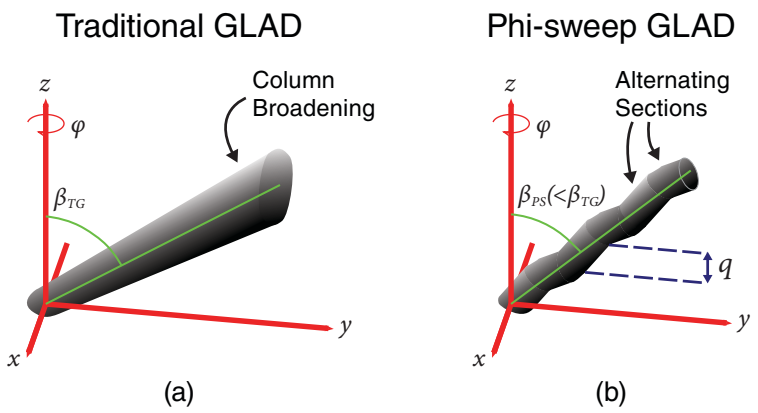

Figure 3.3: Schematic of a) a traditional GLAD column and b) a column produced by the phi-sweep technique. β_{TG} and β_{PS} are the column tilt angles of the traditional GLAD column and the phi-sweep column, respectively, and q is the sweep pitch.

using traditional GLAD.

Recently, Ye *et al.* used a modification of the originally reported phi-sweep process to deposit Si nanostructures onto patterned substrates [66]. Their patterned substrates consisted of 450 nm high tungsten nano-pillars arranged in a square lattice with a lattice constant of 1 μm, and a triangular lattice with a lattice constant of 700 nm. This work is conducted on tetragonal lattices for the development of square spiral photonic crystal materials and devices. Furthermore, we investigate the use of substantially smaller pattern geometries over a range of periodicities and implement the use of TiO_2, as well as Si.

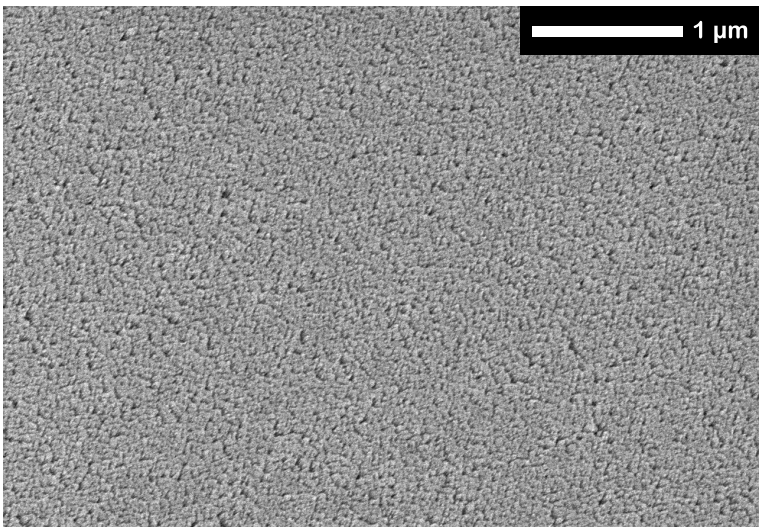

(a)

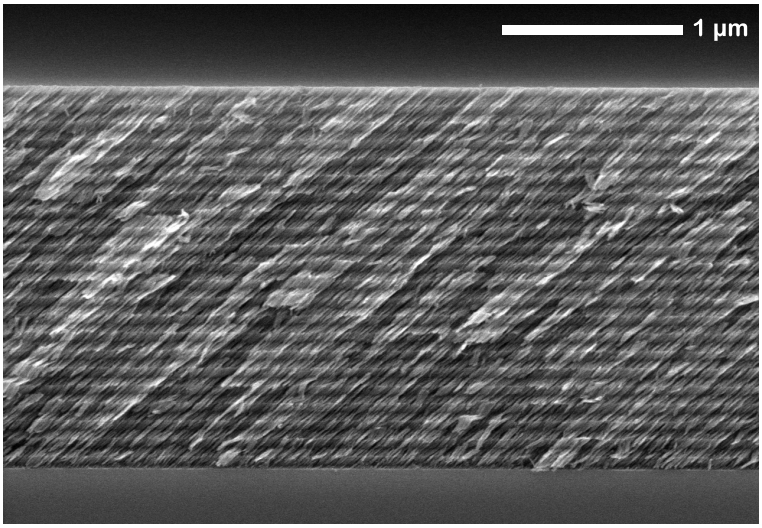

(b)

Figure 3.4: SEM images of the a) top and b) side of a silicon film grown using phi-sweep. The film was grown with a deposition angle of 82°, a sweep pitch of 45 nm, and a sweep angle of 45°.

3.2 Experimental Procedure

In order to grow periodic arrays of slanted columns using GLAD, the substrate must be pre-patterned with an array of small bumps which serve to nucleate the growth of the columns. In this study, a patterned layer of Calix[6]arene negative-tone electron beam resist on a silicon substrate was prepared in collaboration with Mark Summers. For each substrate, the 60 nm thick Calix[6]arene layer was patterned with a Raith 150 electron beam lithography system. The pattern consisted of a two-dimensional square lattice of small hillocks. Three different lattice constants were used: 100, 200, and 300 nm. Each hillock was roughly square shaped, and the length of their sides were approximately 30, 60, and 85 nm for the 100, 200, and 300 nm periodicity patterns, respectively. Top down images of the patterned substrates are shown in Fig. 3.5.

The patterned substrates were loaded on a motor controlled substrate holder 42 cm above the electron beam crucible. The vapour source materials used in this study were Si from Cerac with a purity of 99.999% and TiO_2 from Cerac with a purity of 99.9%. The chamber was evacuated to base pressures of approximately 9×10^{-5} Pa by cryogenic pumping. For the TiO_2 films, after the base pressure was reached, the chamber pressure was increased to 7×10^{-3} Pa by the addition of oxygen near the substrate surface. The background oxygen pressure was essential to achieving adequate oxygen content in the TiO_2 films. Deposition of Si and TiO_2 was performed by electron beam evaporation, and the substrate was tilted so that the deposition angle, α, was 84°. The deposition rate was measured by a quartz crystal oscillator and kept at 15-20 Å/s. After the deposition process, the samples were cleaved and imaged by scanning electron microscopy (SEM). The tilt angles of the slanted columns were measured from the SEM images of each film's

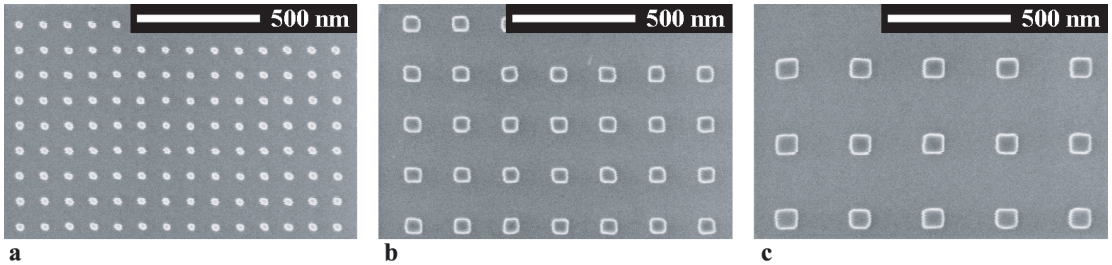

Figure 3.5: Top down SEM images of the **a)** 100, **b)** 200, and **c)** 300 nm periodicity patterned substrates.

cross-section.

Five sets of films were grown, each consisting of three samples: one on each of the 100, 200, and 300 nm periodicity patterned substrates. Three of the sets were grown with Si. The first was grown using traditional GLAD, the second used phi-sweep with a sweep angle, γ, of 30°, and the third used phi-sweep with $\gamma = 45°$. Two sets were grown with TiO_2. The first used traditional GLAD, and the second used phi-sweep with $\gamma = 45°$. All three sets of phi-sweep samples were grown using a sweep pitch, q, of approximately 45 nm.

3.3 Results and Discussion

3.3.1 Phi-Sweep Slanted Post Tilt Angle Derivation

The angle between the column axis and the substrate normal of slanted posts fabricated using traditional GLAD, β_{TG}, is a function of the deposition angle, α. This dependence can be described using the geometrically derived Tait's rule, given in Eq. (3.1) [22].

$$\beta_{TG} = \alpha - \arcsin\left(\frac{1-\cos\alpha}{2}\right) \tag{3.1}$$

The tilt angle of a slanted column grown using the phi-sweep method will differ from that predicted by Tait's rule because the rapid sweeping motion of the phi-sweep method effectively decouples the column growth direction and the direction of incoming vapour flux. The rotations are completed sufficiently quickly so that very little deposition occurs while the substrate is moving. Thus, a slanted post grown using phi-sweep can be approximated as several small linear segments, each one sweep pitch in height. These segments are grown each time the substrate is held in position between the substrate rotations. Each of these small segments will grow toward the source of vapour flux, and will have a tilt angle of β_{TG}. From the substrate's point of view, since the vapour flux direction is alternating between $\phi = +\gamma$ and $\phi = -\gamma$ every substrate sweep, the average growth direction of the slanted post will be in the center of the sweeping motion in the $\phi = 0°$ direction.

Consider a vector $\vec{a}$ of length $|a|$ pointing along the column axis of the first segment of a phi-sweep slanted post. If the substrate is in the x–y plane, and the y-axis is chosen as the desired tilt direction for the slanted post, then $\vec{a}$ is rotated by $+\gamma$ in the ϕ-direction from the y-axis. The angle between the substrate normal, in this case the z-axis, and the

column axis, $\vec{a}$, is given by β_{TG}. The second phi-sweep segment can then be described by a vector $\vec{b}$ of length $|a|$ that is also separated from the z-axis by β_{TG}, but is rotated by $-\gamma$ from the y-axis. The effective growth direction of these two segments, which is the column axis of the phi-sweep slanted post, is given by vector $\vec{c}$, the sum of $\vec{a}$ and $\vec{b}$. The vectors $\vec{a}$, $\vec{b}$, and $\vec{c}$ are described in Cartesian coordinates in Eqs. (3.2), (3.3), and (3.4), respectively.

$$\vec{a} = |a| \sin\beta_{TG} \sin\gamma\ \hat{x} + |a| \sin\beta_{TG} \cos\gamma\ \hat{y} + |a| \cos\beta_{TG}\ \hat{z} \tag{3.2}$$

$$\vec{b} = -|a| \sin\beta_{TG} \sin\gamma\ \hat{x} + |a| \sin\beta_{TG} \cos\gamma\ \hat{y} + |a| \cos\beta_{TG}\ \hat{z} \tag{3.3}$$

$$\vec{c} = \vec{a} + \vec{b} \tag{3.4}$$

After substitution of Eqs. (3.2) and (3.3) into Eq. (3.4), the x-components cancel, as shown in Eq. (3.5), and $\vec{c}$ is in the y–z plane, as shown in Fig. 3.6. The column tilt angle of the phi-sweep slanted post, β_{PS}, is the angle between $\vec{c}$ and the z-axis. The tangent of β_{PS} is given in Eq. (3.6). After cancellation and simplification, the relationship between β_{PS}, β_{TG}, and γ is given by Eq. (3.7). The phi-sweep column tilt angle is not dependent on the length of the phi-sweep segments, $|a|$, and is therefore independent of the sweep pitch, q.

$$\vec{c} = 2|a| \sin\beta_{TG} \cos\gamma\ \hat{y} + 2|a| \cos\beta_{TG}\ \hat{z} \tag{3.5}$$

$$\tan\beta_{PS} = \frac{2|a| \sin\beta_{TG} \cos\gamma}{2|a| \cos\beta_{TG}} \tag{3.6}$$

$$\tan\beta_{PS} = \tan\beta_{TG} \cos\gamma \tag{3.7}$$

The phi-sweep column tilt angle, β_{PS}, can be expressed as a function of α and γ by substituting Tait's rule, Eq. (3.1), for β_{TG} in Eq. (3.7). Figure 3.7 shows the modified Tait's rule for phi-sweep at various sweep angles between 0°, which is equivalent to traditional GLAD, and 90°, which is equivalent to a vertical chevron structure. This plot shows that as the sweep angle increases, β_{PS} decreases, which corresponds to the posts becoming more vertical.

3.3.2 Measured Tilt Angles of Si and TiO_2 Slanted Posts on Patterned Substrates

The Si and TiO_2 samples were cleaved and imaged with SEM. The tilt angle of the columns for each sample was measured from the side view images. The side view SEM images of

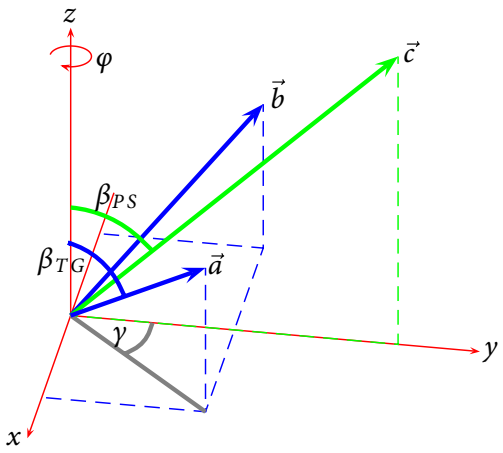

Figure 3.6: Phi-sweep β derivation model.

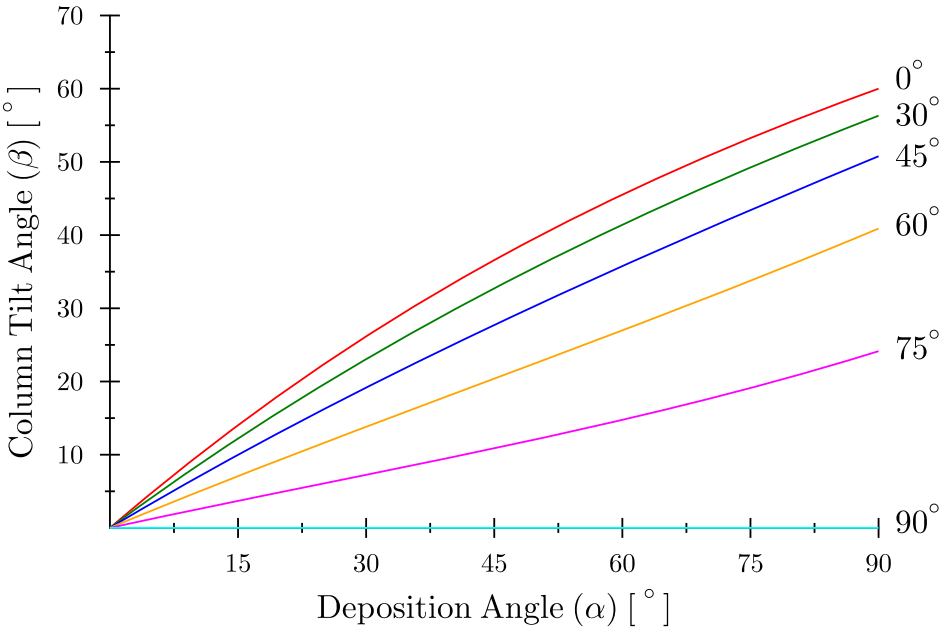

Figure 3.7: Column tilt angle, β, as a function of deposition angle, α, for various sweep angles, γ.

the Si samples are shown in Fig. 3.8. The tilt angle of the columns can be seen to slightly increase with the sweep angle. The column diameter increases with the sample periodicity, which is a necessity of maintaining the same deposition angle, and consequently the same film density. The rippling in the columns caused by the phi-sweep technique is more obvious in the smaller periodicity samples since the column diameter is comparable to the sweep pitch, causing each column growth segment to be clearly visible. The rippling is also more pronounced in the samples with a higher sweep angle of 45° compared to those with a sweep angle of 30°. This makes sense since a higher sweep angle causes the growth segments form a more jagged, zig-zag structure, while as the sweep angle approaches 0°, the column becomes a traditional slanted post for which there is no rippling.

The measurements of the column tilt angles for the Si and TiO_2 samples are given in Tables 3.1 and 3.2, respectively. The values for the measured tilt angles in Tables 3.1 and 3.2 were obtained by measuring the tilt angle of several columns and averaging them for each sample. The uncertainties given are the standard deviation of the measured column tilt angles for each sample. The different periodicity patterned substrates did not have a large effect on the measured tilt angles of the films deposited with the same sweep angle. Equation (3.7) was used to obtain a predicted value for the tilt angle of the phi-sweep films, and these are given in Tables 3.1 and 3.2 for the Si and TiO_2 phi-sweep films, respectively. The predicted values have uncertainty because they are calculated from the measured tilt angle of the traditional GLAD sample. In all cases, the measured and predicted values agreed within error. The phi-sweep films became more vertical with increasing sweep angle, as Fig. 3.7 predicted. Possible errors in the column tilt angle measurement may be due to misalignment of the column tilt direction with the substrate cleave, misalignment of the sample during SEM imaging, or misalignment of the sample on the substrate holder during the film deposition. These misalignments would affect the measured tilt angles.

One of the advantages of the phi-sweep method can be seen from the top down SEM images of the Si samples in Fig. 3.9, and the oblique view SEM images of the TiO_2 films in Figure 3.10. The traditional GLAD method, as seen in Figs. 3.9a, b, and c, resulted in columns that fanned out so their cross-sections became highly elliptical. In the case of the 200 and 300 nm periodicities, the columns even merged into long ribbon-like structures. The phi-sweep process prevents this column fanning because it increases the uniformity of the flux arrival and breaks the anisotropy in the shadowing conditions.

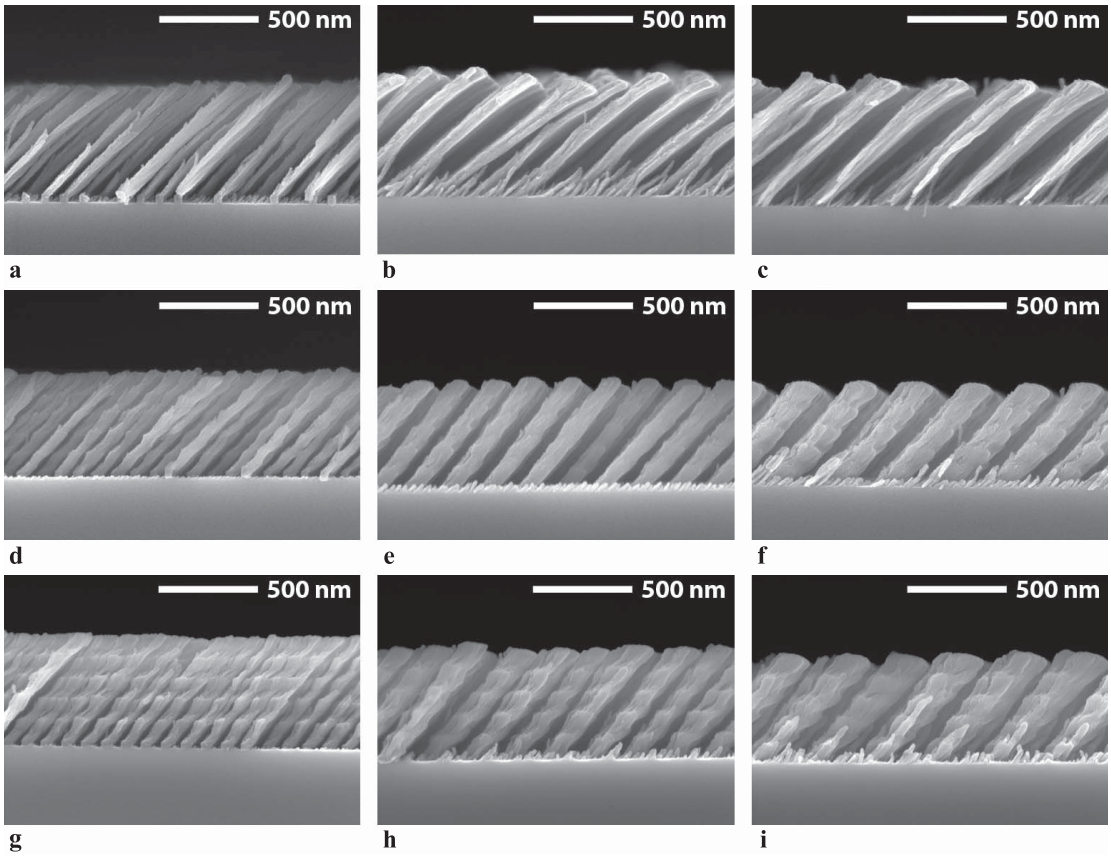

Figure 3.8: Side view SEM images of the Si slanted post films fabricated using **a)**, **b)**, **c)** traditional GLAD, **d)**, **e)**, **f)** phi-sweep with a sweep angle of 30°, and **g)**, **h)**, **i)** phi-sweep with a sweep angle of 45° on 100, 200, and 300 nm periodicity substrates, respectively.

γ (°)	Measured β (°)				Predicted β (°)
	Patterned Regions			Average	
	100 nm	200 nm	300 nm		
0	48 ± 3	48 ± 3	48 ± 2	48 ± 2	N/A
30	44 ± 2	42 ± 3	43 ± 2	43 ± 3	44 ± 2
45	38 ± 2	39 ± 2	40 ± 2	39 ± 2	38 ± 2

Table 3.1: Measured and predicted column tilt angles, β, of Si slanted post films deposited with sweep angles, γ, of 0°, 30°, and 45°. The column tilt angles were independently measured on the 100, 200, and 300 nm periodicity patterned substrates.

γ (°)	Measured β (°)				Predicted β (°)
	Patterned Regions			Average	
	100 nm	200 nm	300 nm		
0	50 ± 3	52 ± 2	52 ± 2	52 ± 2	N/A
45	41 ± 2	43 ± 2	41 ± 2	42 ± 2	42 ± 2

Table 3.2: Measured and predicted column tilt angles, β, of TiO_2 slanted post films deposited with sweep angles, γ, of 0° and 45°. The column tilt angles were independently measured on the 100, 200, and 300 nm periodicity patterned substrates.

Figures 3.9d, e, and f show that the phi-sweep technique resulted in slanted columns with a more circular cross-section. These results agree with those reported on larger seed geometries by Jensen and Brett using phi-sweep [43], and by Ye *et al.* using their modified phi-sweep technique [66]. The films produced with the phi-sweep method retained periodicity in both directions, and the columns were separated much better than in the films produced using traditional GLAD. We have shown here that the phi-sweep technique has increased the range of size scales over which periodic nanostructures can be grown by GLAD, down to 100 nm periodicity.

The column tilt angles measured here are not the optimum values of 64° and 79° for the ideal [001]-diamond:1 and [001]-diamond:5 square spiral structures, respectively. Although the column tilt angles can be increased by using a larger deposition angle, Fig. 3.7 shows that the maximum tilt angle attainable by GLAD is approximately 60°. This suggests that the [001]-diamond:5 structure may be out of reach of current GLAD technology, but the optimum [001]-diamond:1 structure is not far off. Many materials vary from what is predicted by Tait's rule, and certain materials may have a higher maximum column tilt angle than 60°. Also, ion bombardment during film growth is being explored as a means to increase the column tilt [67, 35]. The value of 64° is only an optimum value, and significant band gaps can still exist in structures with lower spiral arm tilt angles [64]. For instance, a [001]-diamond:1 square spiral with an tilt angle of 56° is predicted to have a band gap of approximately 10% the center frequency [64], and Jensen and Brett have recently reported a [001]-diamond:1 silicon square spiral that was deposited with α = 85° to have a measured band gap of 10.9% [43]. One disadvantage of the phi-sweep technique is that it reduces the column tilt angle further from the ideal value, so there is a compromise between a higher column tilt angle and a more circular column cross-section.

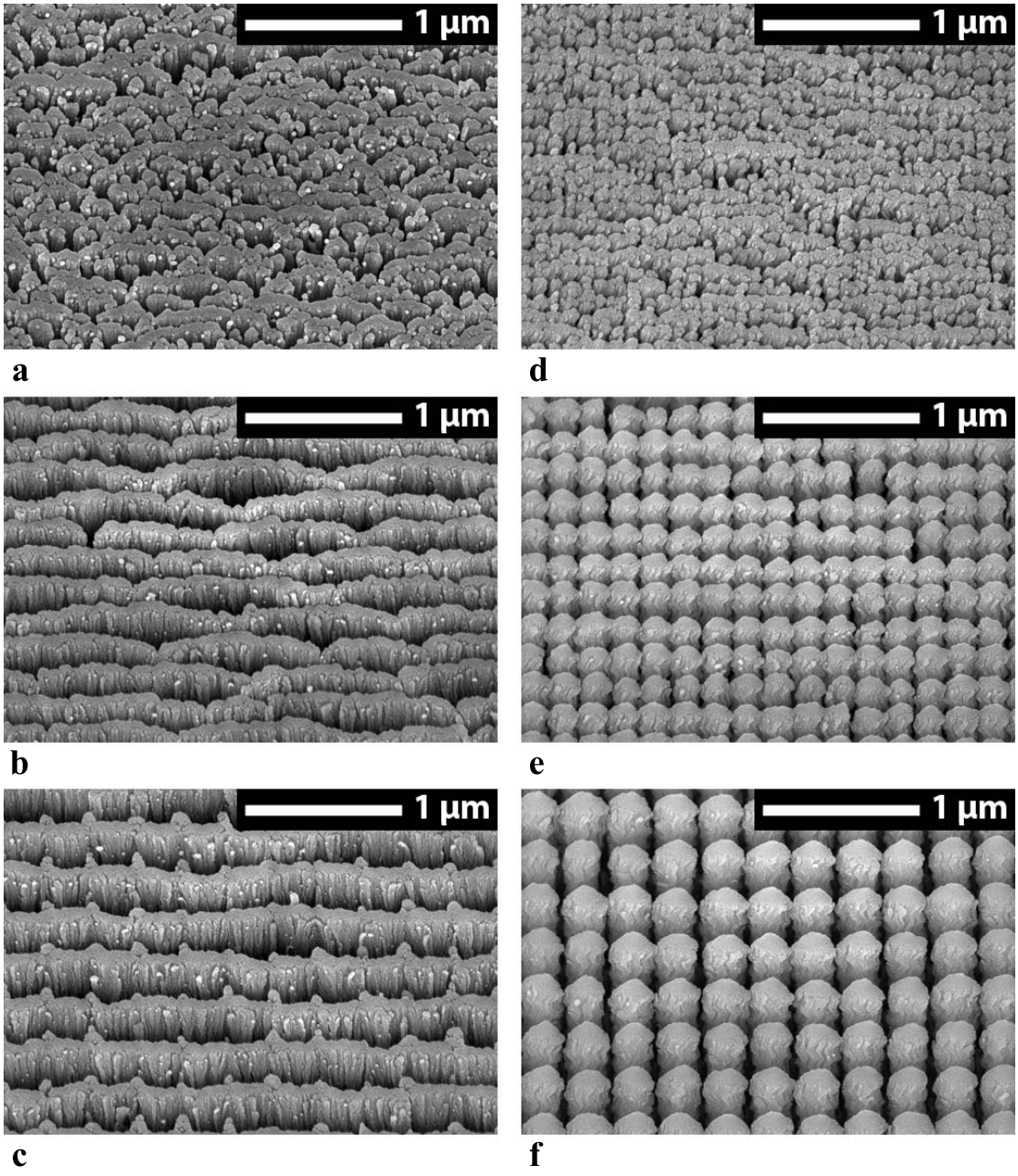

Figure 3.9: Top view SEM images of the Si slanted post films fabricated using **a)**, **b)**, **c)** traditional GLAD and **d)**, **e)**, **f)** phi-sweep with a sweep angle of 30° on 100, 200, and 300 nm periodicity substrates, respectively.

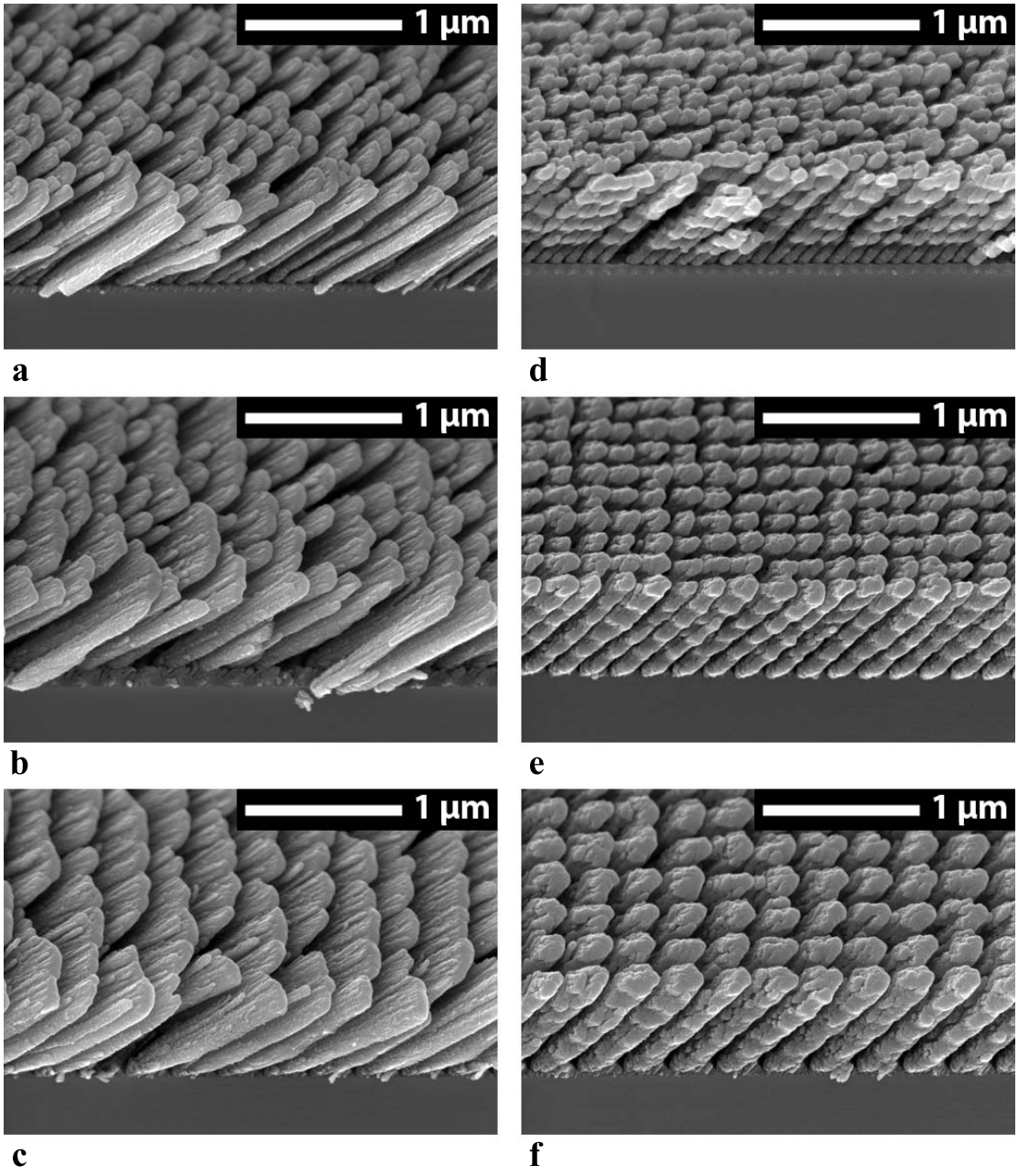

Figure 3.10: Oblique view SEM images taken at 45° from the substrate normal of the TiO_2 slanted post films fabricated using **a)**, **b)**, **c)** traditional GLAD and **d)**, **e)**, **f)** phi-sweep with a sweep angle of 45° on 100, 200, and 300 nm periodicity substrates, respectively.

3.4 Conclusion

Advanced substrate motion in the phi-sweep modification to the glancing angle deposition process improves the structure of square spiral photonic crystals. It is known that the properties of these photonic crystals are affected by the tilt angle of the square spiral arms. However, the phi-sweep method changes the tilt angle of the linear segments in the square spirals, and it is important to understand how. We have derived the relationship between the phi-sweep parameters and the column tilt angle of phi-sweep slanted columns. The tilt angle is a function of the sweep angle, γ, and the deposition angle, α, but not the sweep pitch, q. As the sweep angle increases, the slanted columns become more vertical. This was confirmed from measured results of Si and TiO_2 films grown on periodically patterned substrates. We also showed that the phi-sweep method substantially reduces the fanning of the columns compared to traditional GLAD. The phi-sweep process produced films that conformed much better to the initial pattern on the periodically patterned substrates, and has extended the range of size scales over which periodic columns can be grown by GLAD.

4 LSPR IN GLAD FILMS

4.1 Introduction

Recently there has been a lot of interest in applications based on the localized surface plasmon resonance (LSPR) of noble metal nanoparticles [68, 69, 70, 71, 72, 73, 74, 75, 76, 77, 78, 79, 80, 81]. The optical response of these particles is typically characterized by the presence of a strong absorption and scattering peak that is not present in the spectrum of the bulk metal. This is due to the coupling of the conduction electrons in the metal to the electromagnetic field of the incident light. The resonance position is dependent on the size and shape of the particles, coupling between the particles, the dielectric properties of the metal, and the dielectric properties of the local environment surrounding the particles [82]. The latter allows for sensing of local refractive index changes by measuring shifts in the peak positions of extinction spectra. By functionalizing the surface of the nanoparticles to bind to a specific analyte, sensitive biosensors can be designed.

4.2 Background and Theory

The interaction of electromagnetic radiation with electrons at a metal-dielectric interface can lead to the resonant excitation of surface plasmon (SP) polaritons. Materials with a negative real and small positive imaginary dielectric constant are capable of supporting a surface plasmon resonance [83]. There are two main types of surface plasmon resonance (SPR): propagating and localized. In propagating surface plasmon resonance (PSPR), surface plasmons are excited and travel along the surface of a planar metal-dielectric interface. Due to momentum matching requirements, it is necessary to use specialized geometries to couple the incident radiation to the surface plasmon resonance. This is typically accomplished using a prism in the Otto or Kretschmann configuration, or with a grating structure [84]. In the second type, localized surface plasmon resonance (LSPR), the SPs are charge density oscillations confined to metal nanostructures or sharp features on the nanometre scale, as illustrated in Figure 4.1. In LSPR, the SPs can be excited and

monitored in the simple transmission mode with no requirement for special coupling geometries.

The optical properties of a spherical particle in some dielectric medium can be modeled using Mie theory. This is an exact solution to Maxwell's equations for a homogeneous spherical particle embedded in an infinitely uniform medium, and was first derived by Gustav Mie in 1908 [85]. However, since the equations contain infinite series of complex equations, it is often more convenient to use an estimation in the long-wavelength, electrostatic dipole limit. This is given by the following equation [83, 86]:

$$E(\lambda) = \frac{24 f a \varepsilon_m^{3/2}}{\lambda \ln(10)} \left[\frac{\varepsilon_i}{(\varepsilon_r + \chi \varepsilon_m)^2 + \varepsilon_i^2} \right] \tag{4.1}$$

where $E(\lambda)$ is the extinction, f is the area fraction occupied by particles, a is the radius of the sphere, ε_m is the dielectric constant of the medium surrounding the sphere, λ is the wavelength, ε_r is the real portion of the particle's dielectric function, ε_i is the imaginary portion of the particle's dielectric function, and χ is the term that describes the aspect ratio of the particle (equal to 2 for a sphere). Extinction (also called absorbance or attenuance) is defined as $E(\lambda) = -\log(T(\lambda))$, where $T(\lambda)$ is the transmittance, and accounts for losses due to both scattering and absorption. It is evident that for a sample of spherical particles where ε_i is relatively constant, there will be a peak in the extinction spectrum when $\varepsilon_r = -2\varepsilon_m$. The values of χ increase for high aspect ratio particles that have their long axis aligned with the incident electric field. Spheres have a χ value of 2, while this increases to 17 for a 5:1 aspect ratio particle [86]. The value of χ can only be solved analytically for spheres and spheroids, and must be approximated for other geometries [83]. The value of χ for a prolate spheroid with minor axis $2a$ and major axis $2b$ where the electric field is aligned with the major axis is given by the following equation [87]:

$$\chi = -1 + \left\{ \left[\frac{\xi_0}{2} \ln\left(\frac{\xi_0 + 1}{\xi_0 - 1} \right) - 1 \right] \left(\xi_0^2 - 1 \right) \right\}^{-1} \tag{4.2}$$

where

$$\xi_0 = \left(1 - \frac{a^2}{b^2} \right)^{-\frac{1}{2}} \tag{4.3}$$

For electric fields parallel to the minor axis of a prolate spheroid, the value of χ is smaller than 2, resulting in plasmon resonances at slightly lower wavelengths than the spherical

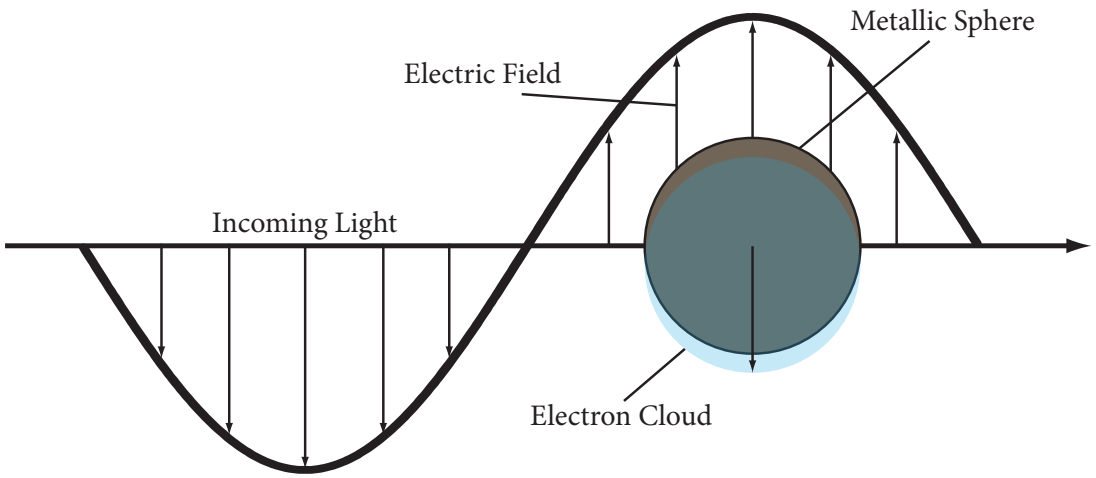

Figure 4.1: Schematic of localized surface plasmon oscillation for a metal sphere. The conduction electron charge cloud is displaced due to the incident electric field.

particle resonance [87].

Equation 4.1 shows a dependence on the nanoparticle radius, the nanoparticle material, the particles' environment, and the particles' shape. Calculated extinction spectra for samples of 50 nm radius silver particles with an area fraction of 0.5 are shown in Fig. 4.2a) in media of various index of refraction, $n = \sqrt{\varepsilon_m}$, with $\chi = 2$ and Fig. 4.2b) using different values for χ in an vacuum medium. Similarly, calculated extinction spectra for samples of 100 nm radius gold particles with an area fraction of 0.5 are shown in Fig. 4.3a) in media of various index of refraction with $\chi = 17$ and Fig. 4.3b) using different values for χ in an vacuum medium. It is evident that due to its dielectric constant, gold has an extinction peak at a higher wavelength than silver. With both materials, the extinction peak red-shifted as the refractive index of the medium increased. The extinction peak also red-shifted with increasing χ values (higher aspect ratio particles).

Both PSPR and LSPR have been under heavy investigation for sensing applications, although the PSPR method is considerably more established, and as such, many commercial PSPR biosensing instruments are available. The sensing mechanism of both methods is reliant on a change in resonance conditions due to a refractive index (RI) variation in the vicinity of the metal-dielectric interface upon analyte binding. The response, R, of either method to the formation of an analyte layer of thickness d on the metal surface is

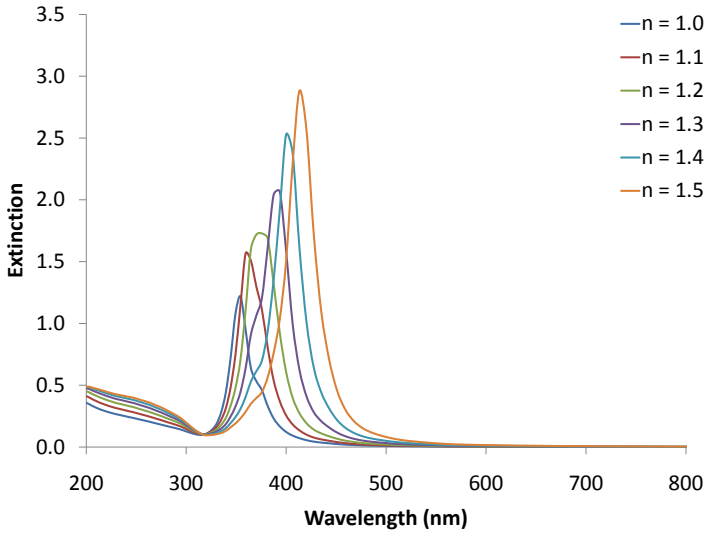

(a)

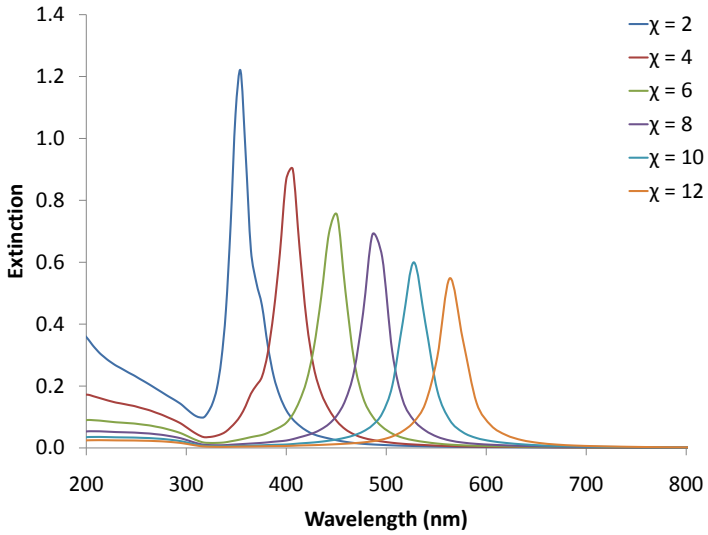

(b)

Figure 4.2: Calculated extinction spectra for samples of 50 nm radius silver particles with an area fraction of 0.5 are shown in a) using media of various index of refraction with $\chi = 2$ and b) using different values for χ in an vacuum medium.

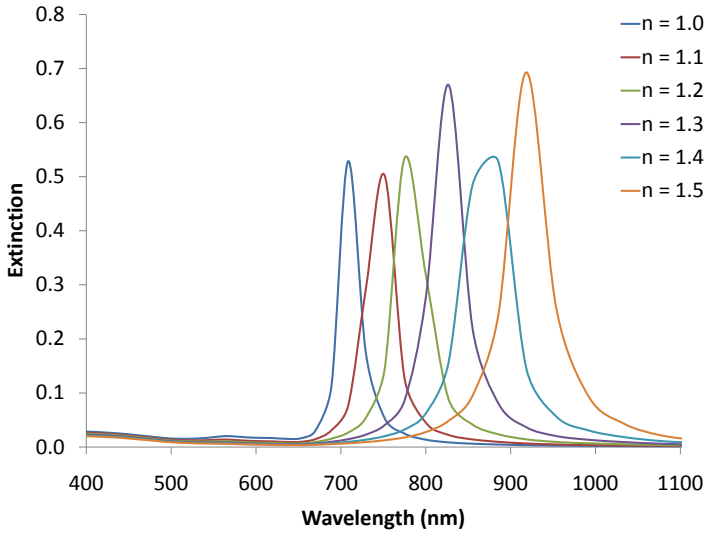

(a)

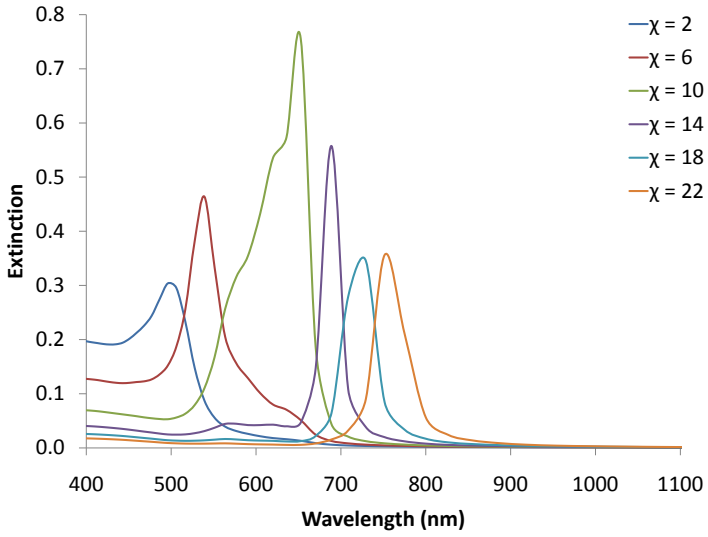

(b)

Figure 4.3: Calculated extinction spectra for samples of 100 nm radius gold particles with an area fraction of 0.5 are shown in a) using media of various index of refraction with $\chi = 17$ and b) using different values for χ in an vacuum medium.

given by:

$$R = m(n_a - n_s)\left[1 - \exp(-2d/L_d)\right] \tag{4.4}$$

where n_a and n_s are the refractive indexes of the analyte layer and the bulk medium, respectively, m is the refractive index sensitivity, and L_d is the decay length of the evanescent field. The response is typically measured as an intensity change or a wavelength shift. The refractive index sensitivity (also called the sensitivity factor), m, is then measured as the intensity change per refractive index unit (RIU), or the wavelength shift per refractive index unit, respectively. Although the RI sensitivity of PSPR based sensors is typically 1–2 orders of magnitude higher than LSPR systems, this is largely made up for by the difference in decay length of the two methods [88]. The decay length of LSPR systems is typically 10–30 nm, whereas L_D for PSPR sensors is normally at least an order of magnitude larger. The sensitivity of the two methods to a thin analyte layer is therefore quite comparable.

When designing SPR biosensors, it is common to include a recognition interface that is placed on the metal surface to enable selective binding to a specific analyte. If the RI of the analyte and the recognition layer are assumed to be the same, n_a, the response equation incorporating such a layer is given by:

$$R = m(n_a - n_s)\exp(-2d_i/L_d)\left[1 - \exp(-2d_a/L_d)\right] \tag{4.5}$$

where d_i and d_a are the thicknesses of the recognition layer and the analyte layer, respectively [89]. It is evident from Eq. 4.5 that a thicker recognition layer will decrease the response, and this decrease will be much greater if the decay length is small. Therefore, the recognition layer thickness is a more important parameter in LSPR sensors than in PSPR sensors.

4.3 Sphere-like Particle Films

To investigate localized surface plasmon resonance in films fabricated by glancing angle deposition, several silver thin films were grown while the substrate was constantly rotated about the phi axis. The films were deposited on fused silica substrates so that their extinction spectra could be measured. The extinction measurements of the samples were taken using a PerkinElmer Lambda 900 UV/VIS/NIR spectrophotometer using standard

transmission geometry with unpolarized light.

An initial batch of films was grown at varying deposition angles of 79°, 81°, 83°, and 85°. Figure 4.4 shows SEM images of these films. Due to the difficulty in estimating the ratio of film thickness to thickness measured by the quartz crystal microbalance (QCM) at different deposition angles, there was a variance in the thicknesses between the films of approximately 100 – 170 nm. Since the porosity and degree of particle isolation in the films were of primary interest, and porosity is independent of film thickness, this was an acceptable variance. At low deposition angles, the films have quite a rough surface, but have no isolated particles. As the deposition angle increases, the porosity of the films also increase until they consist of more isolated, sphere-like particles.

The extinction spectra of these films can be seen in Fig 4.5. At low deposition angle, there is no prominent extinction peak. As the deposition angle is increased slightly, an extinction peak becomes evident in the spectra due to localized surface plasmon resonance. Further increases in the deposition angle cause the extinction peak to blue-shift as the particles become more isolated. The minimum at approximately 320 nm is due to intraband transitions in the silver metal that damps the plasma oscillations [90].

A deposition angle of 85° was chosen for the next set of experiments since the SEM images of the silver films showed the best particle isolation at this angle and there was a prominent, sharp peak in the extinction spectra. A batch of silver films of different thicknesses was grown at a deposition angle of 85° using constant phi-rotation varying between 4 nm and 177 nm thick. The ratio between film thickness and thickness measured by the QCM was determined for silver at a deposition angle of 85° using the measured film thicknesses from side-view SEM images of several samples that were thicker than 100 nm. Due to the variation in particle height, the film thickness is not obviously defined. Here the film thickness is defined as the average height of the dominant features in the film, and was manually measured from the SEM images. A sample of one of these side-view SEM images is shown in Fig. 4.6. This ratio was then used to estimate the thickness of thinner films for which side-view SEM images were not of high enough resolution to obtain accurate measurements. Figure 4.5 shows SEM images of films that are 4 nm, 14 nm, 150 nm, and 177 nm thick.

The extinction spectra of several films of different thicknesses are shown in Fig. 4.7. The thinnest films have an extinction peak at approximately 430 nm. Starting with the 35 nm film, a second peak appears around a smaller wavelength of approximately 370 nm.

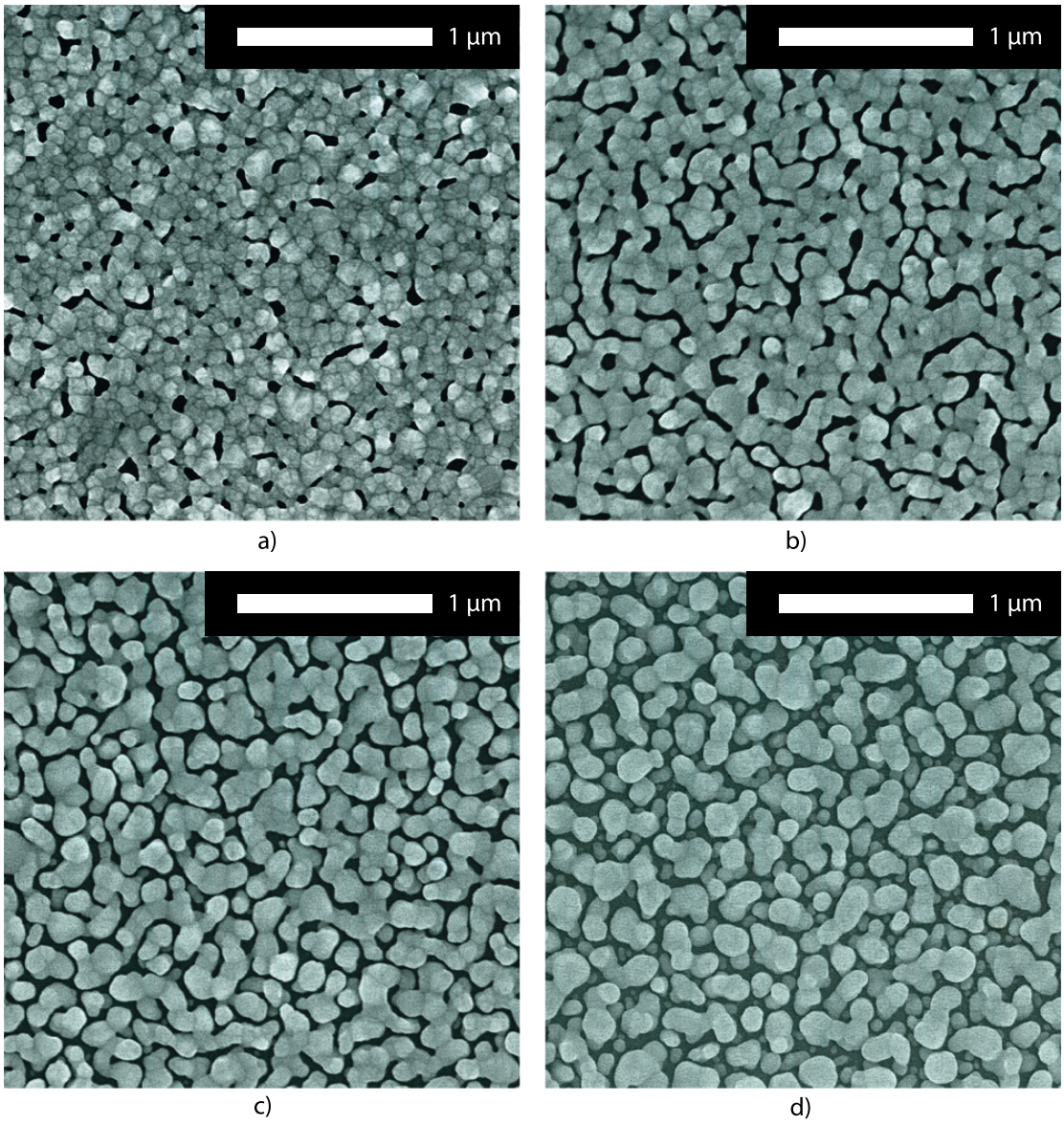

Figure 4.4: SEM images of four silver samples grown using constant phi-rotation at deposition angles of a) 79°, b) 81°, c) 83°, and d) 85°.

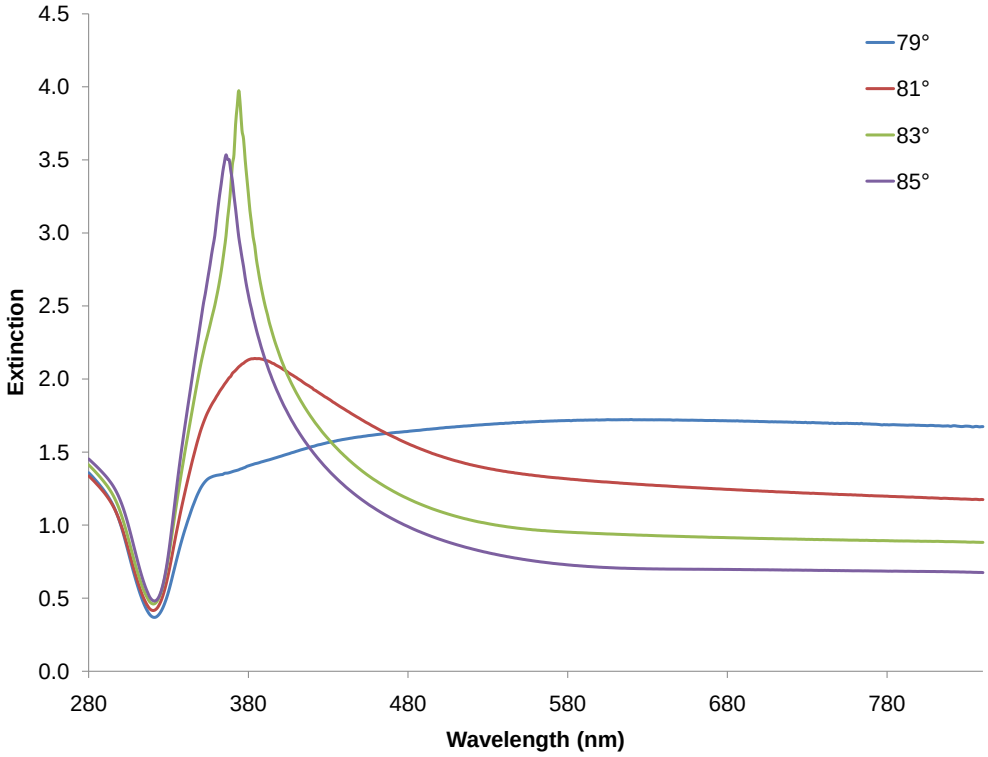

Figure 4.5: Extinction spectra of four silver samples grown using constant phi-rotation at different deposition angles.

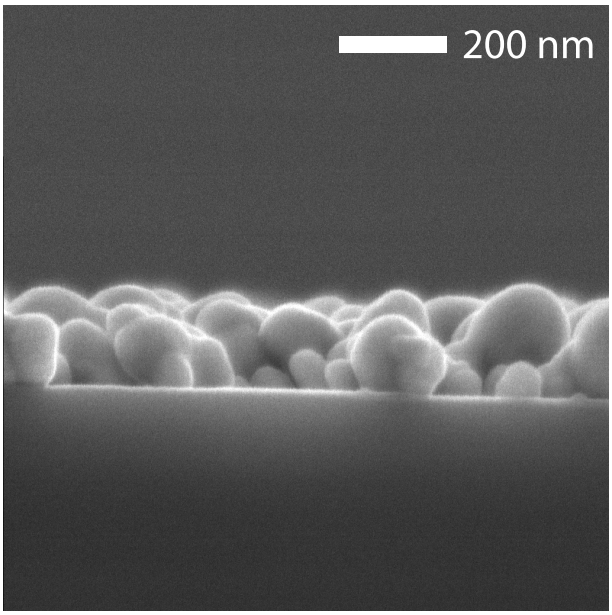

Figure 4.6: Side-view SEM image of a 177 nm thick silver film grown using constant phi-rotation.

This may be an effect of the substrate, since the position of the extinction peak of the samples with smaller particles that are closer to the substrate match up well with the calculated peak location with $n = 1.5$ in Fig. 4.2a, while the spectra of the larger particles that are centered further away from the substrate match up well with the peak calculated for $n = 1$. For the 35 nm thick film, the particles may support resonances at two different peaks, one localized near the top of the particle, away from the substrate, and one near the bottom, adjacent to the substrate. The two peaks may also be attributed to quadrapole or higher mode resonances which can get excited in larger particles [90, 91]. In increasingly thicker films, the shorter wavelength peak becomes dominant.

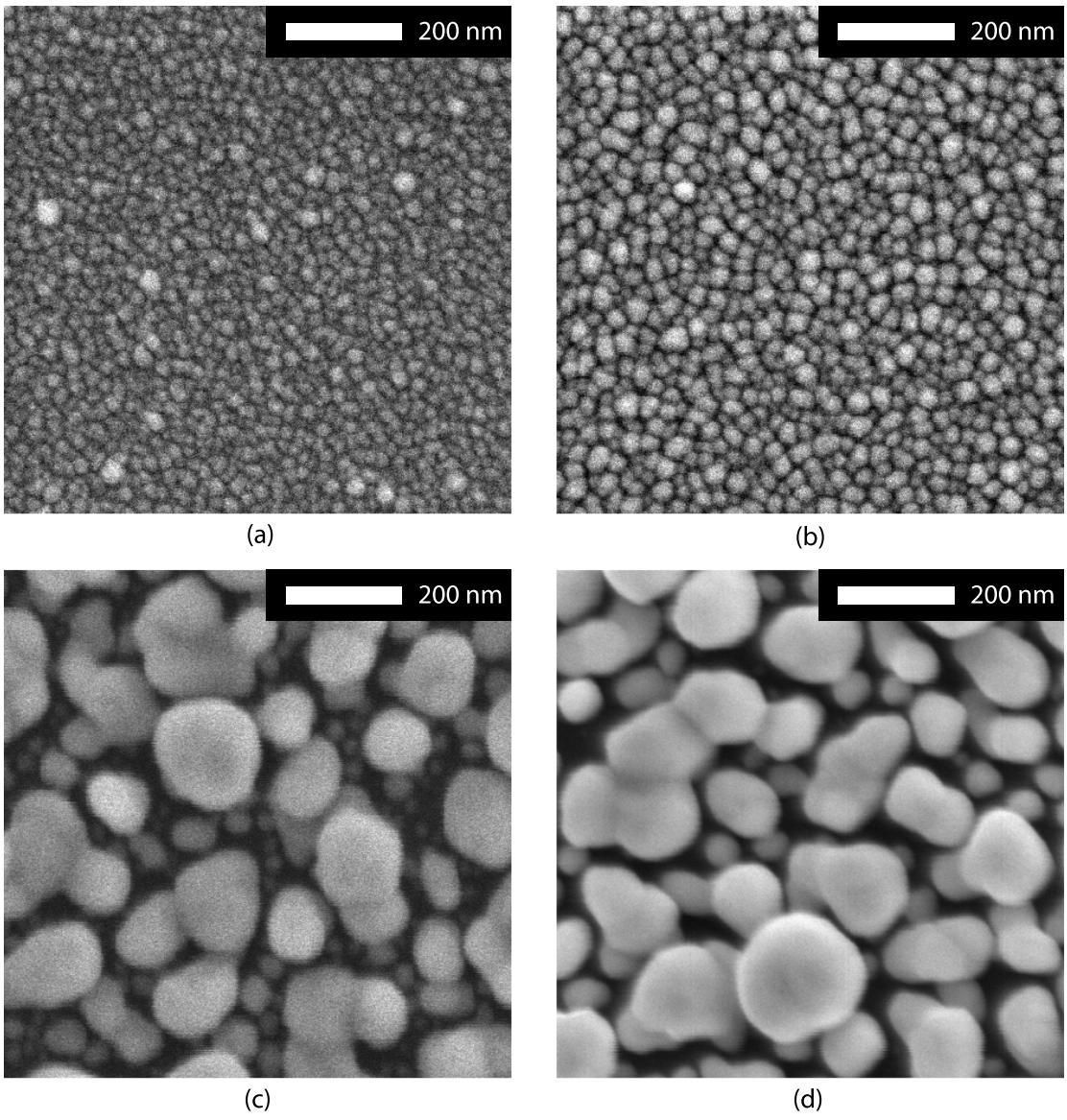

Figure 4.7: SEM images of four silver samples grown using constant phi-rotation with thicknesses of a) 4 nm, b) 14 nm, c) 150 nm, and d) 177 nm.

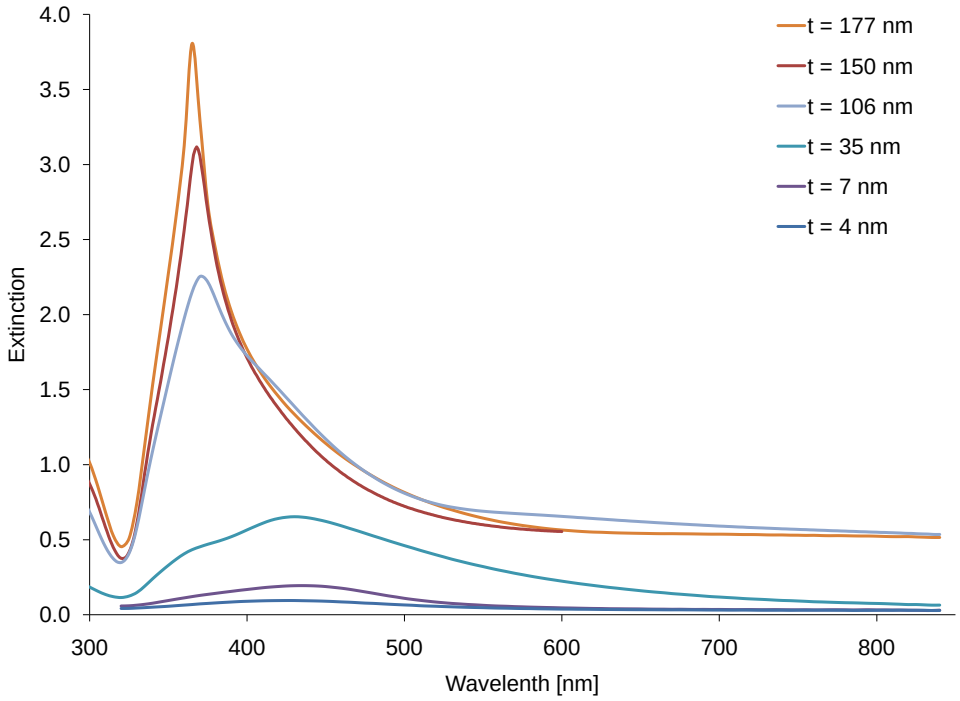

Figure 4.8: Extinction spectra of silver samples grown using constant phi-rotation with different thicknesses.

4.4 Slanted Post Films

Samples consisting of high aspect ratio particles will have two resonant peaks at different wavelengths. The higher energy, shorter wavelength peak is due to plasmon excitation along the short axis of the anisotropic particles, while the lower energy, longer wavelength peak is due to excitation along the long axis. These two modes are referred to as the transverse and longitudinal modes, respectively. These effects should be evident in noble metal GLAD films consisting of high aspect ratio particles, such as slanted post GLAD films.

A deposition was carried out in which six different slanted post films were grown at a deposition angle of 86°. Each film was positioned at a different distance from the source material, and therefore accumulated a different final post length. The SEM images of the six samples are shown in Figure 4.9. The average post length of the six samples was measured from the top-down SEM images to be 62±4 nm, 98±3 nm, 111±4 nm, 138±5 nm, 174 ± 8 nm, and 198 ± 7 nm. The lengths of 20 posts were measured and averaged for each sample. The error given is the standard deviation of the mean. From the side-view SEM image of the sample with an average post length of 198 nm, shown in Figure 4.10, we can see that the posts are tilted over at an angle of approximately 65° to 70° from the substrate normal. Since the posts are not actually lying flat on the substrate, the measured lengths from the top-down images are actually the lengths of the posts' projection on the substrate. The actual post lengths are 6 to 10 % higher than their projection on the substrate. However, for the purpose of this discussion the measured projected lengths from the top-down images will be referred to as the post lengths. The average post length of each sample plotted against its distance from the source material during the deposition is shown in Figure 4.11. The average post length of a sample decreases linearly as its distance from the source during the deposition increases.

In GLAD slanted post films, the posts all tilt in the same direction, making the sample anisotropic. Because of this, there will be a linear polarization dependence in the localized surface plasmon resonance. By using polarized light for the extinction measurement, where the electric field is aligned either along the posts' tilt direction or perpendicular to it, either the longitudinal plasmon mode or the transverse plasmon mode, respectively, can be selectively excited. The longitudinal extinction spectra for the six samples are shown in Figure 4.12a, while the transverse extinction spectra are shown

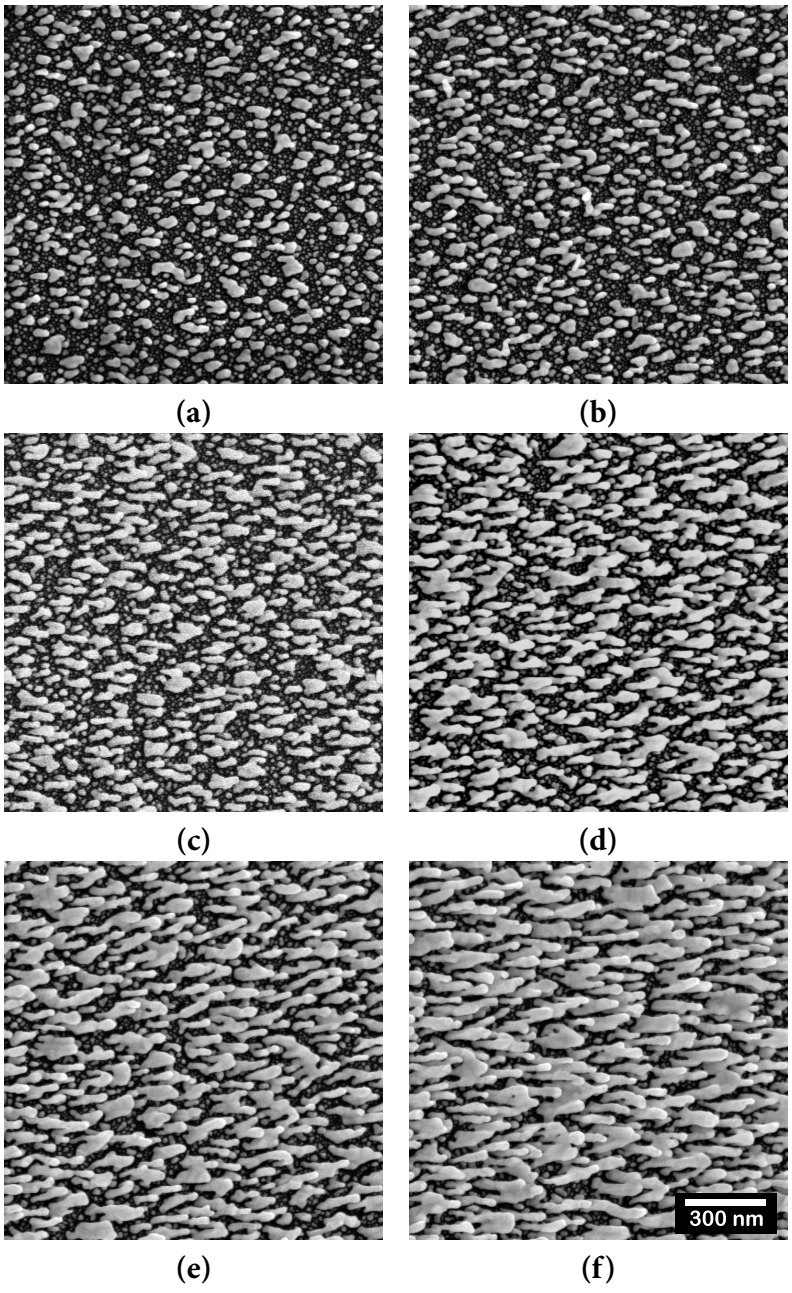

Figure 4.9: SEM images of gold slanted post films. The average post length for each sample is a) 62 nm, b) 98 nm, c) 111 nm, d) 138 nm, e) 174 nm, and f) 198 nm.

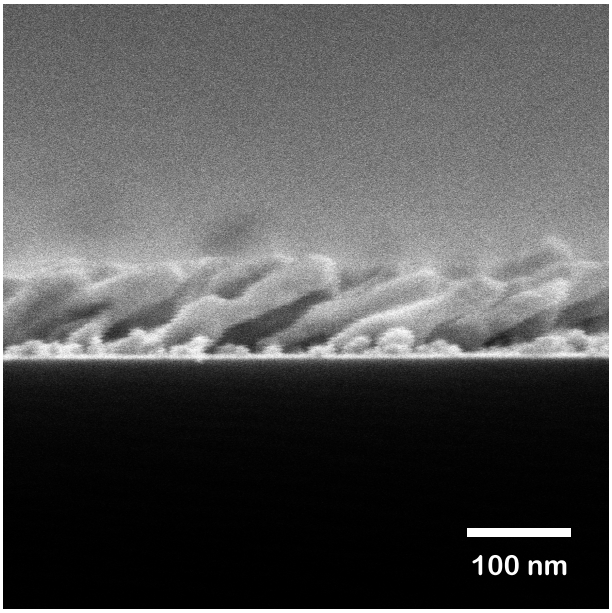

Figure 4.10: Side-view SEM image of 198 nm average length gold slanted post sample.

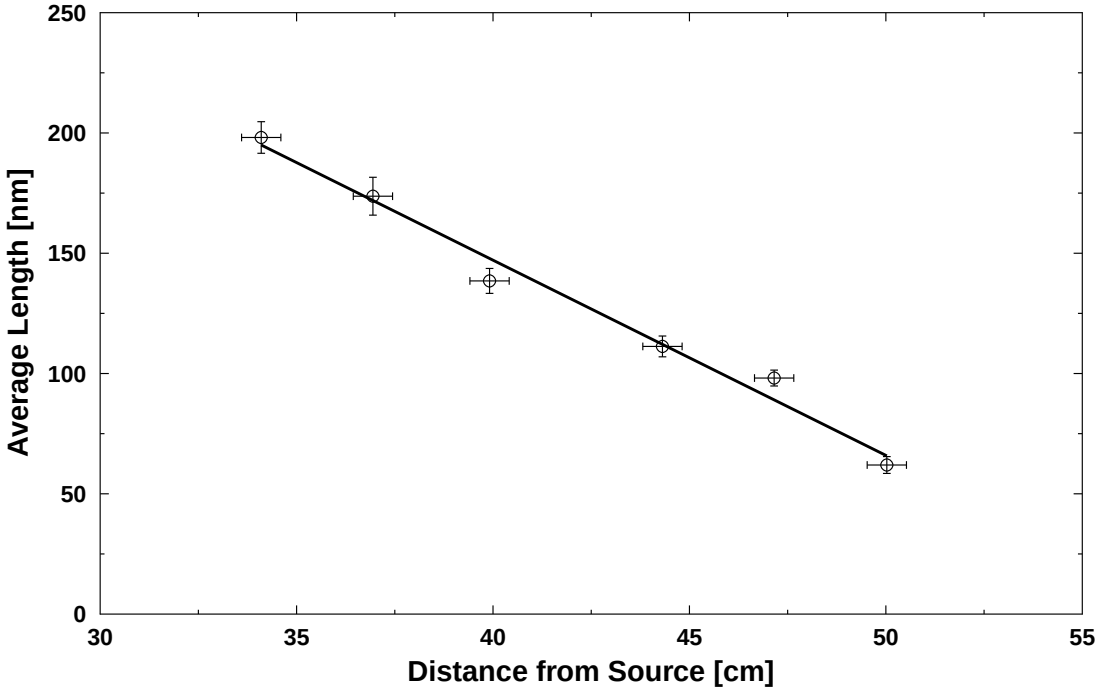

Figure 4.11: Length of gold slanted posts for samples grown at different distances from the source material.

in Figure 4.13a. As expected, the longitudinal extinction peak occurs at a lower energy, or higher wavelength than the transverse peak. The longitudinal peaks are also substantially broader than the transverse peaks. The resonant wavelength for both the longitudinal and transverse modes is plotted against the average post lengths in Figure 4.14. As the post length increases, the position of the longitudinal extinction peak linearly redshifts quite significantly, while the transverse peak slightly blue shifts.

The sensitivity of the longitudinal and transverse extinction peaks to changes in the refractive index of the surrounding media is also quite different. To measure the samples' sensitivities, their extinction spectra were measured while being immersed in water using a cuvette. The background scans for the measurements were taken with an cuvette filled with water in the beam path to account for extinction due to water absorption. The longitudinal and transverse extinction spectra of the six samples are shown in Figures 4.12b and 4.13b, respectively. The calculated sensitivity of each sample for the the longitudinal and transverse peaks is shown in Figure 4.15. The sensitivity of the longitudinal peaks are much higher than the transverse peaks. In addition, the sensitivity of the longitudinal peak increases linearly with the average length of the posts, whereas the sensitivity of the transverse peak seems to be somewhat independent of the average post length. This can be qualitatively understood from Eq. 4.1 where, for relatively constant ε_i, the extinction peak occurs when $\varepsilon_r(\lambda) = -\chi\varepsilon_m$. The value of χ magnifies the effect of changes in the dielectric constant of the surrounding medium, ε_m. When the electric field is parallel to the long axis of the particles, χ is large, and the extinction peak position is more sensitive to changes in ε_m. When the electric field is parallel to the small axis of the particles, χ is small and the peak position is less sensitive to the index of its surrounding medium.

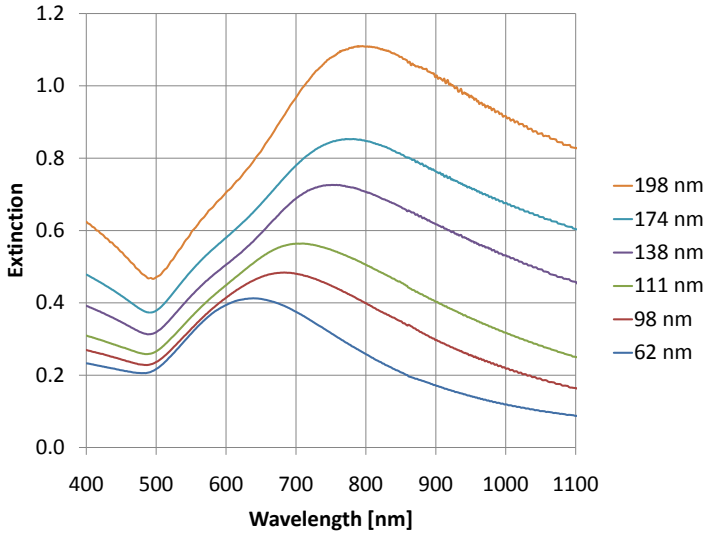

(a)

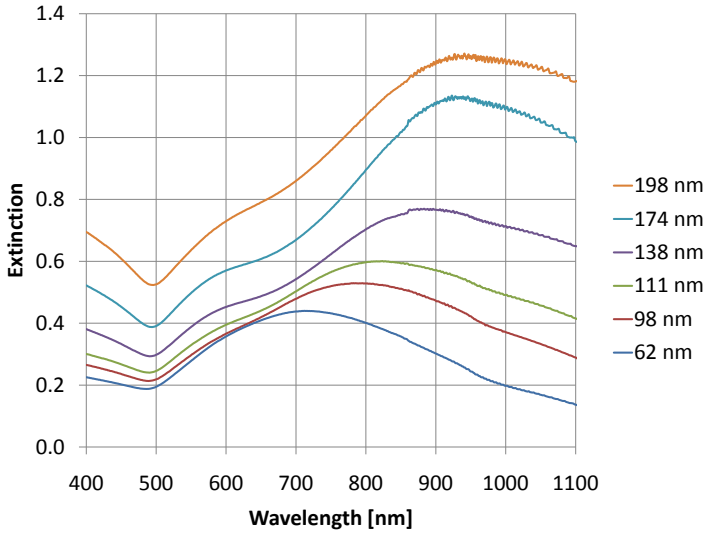

(b)

Figure 4.12: Longitudinal extinction spectra of gold slanted post films of different average lengths in a) air and b) water.

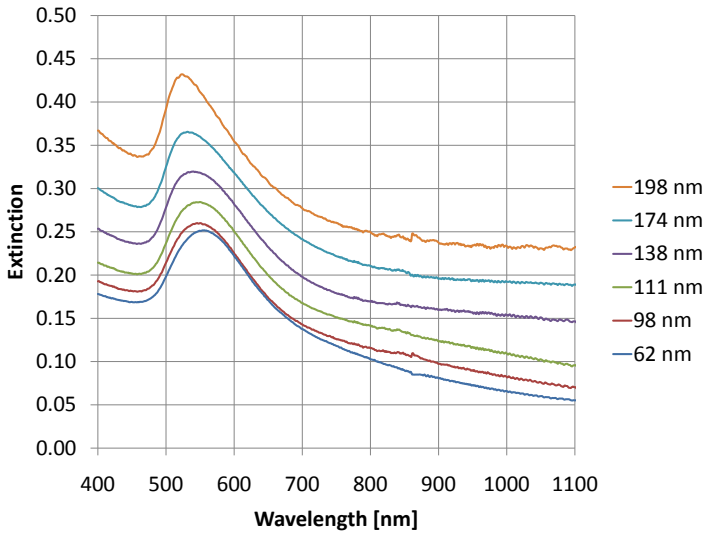

(a)

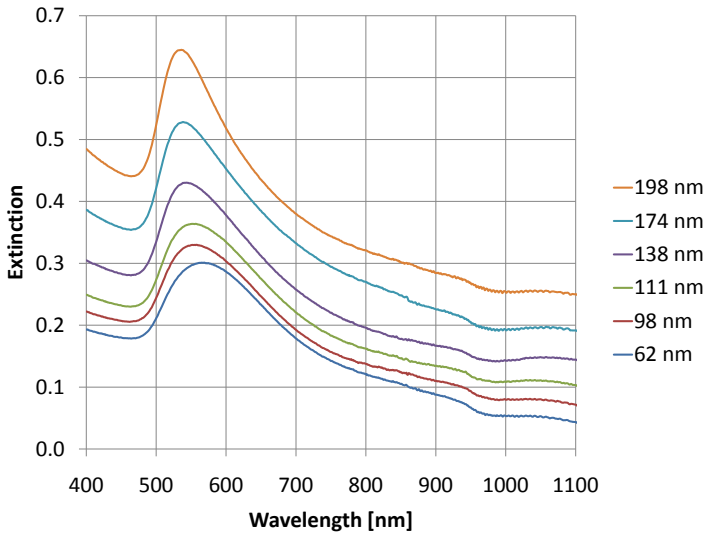

(b)

Figure 4.13: Transverse extinction spectra of gold slanted post films of different average lengths in a) air and b) water.

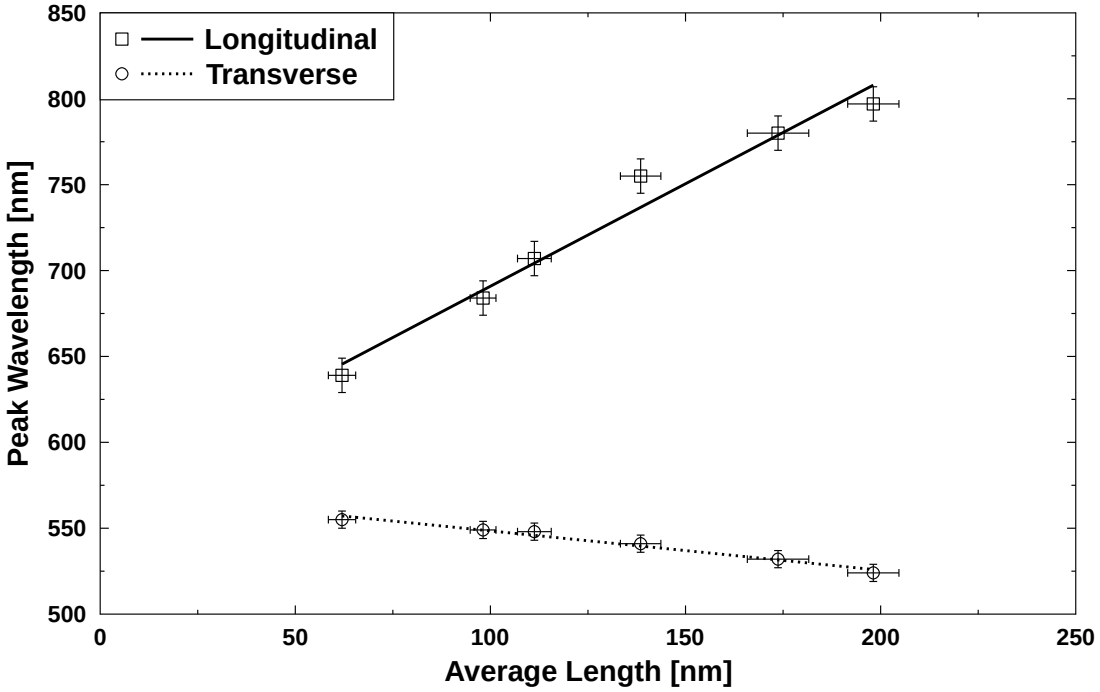

Figure 4.14: Localized surface plasmon resonant wavelength of gold slanted post samples with different average post lengths for both the transverse and longitudinal polarizations.

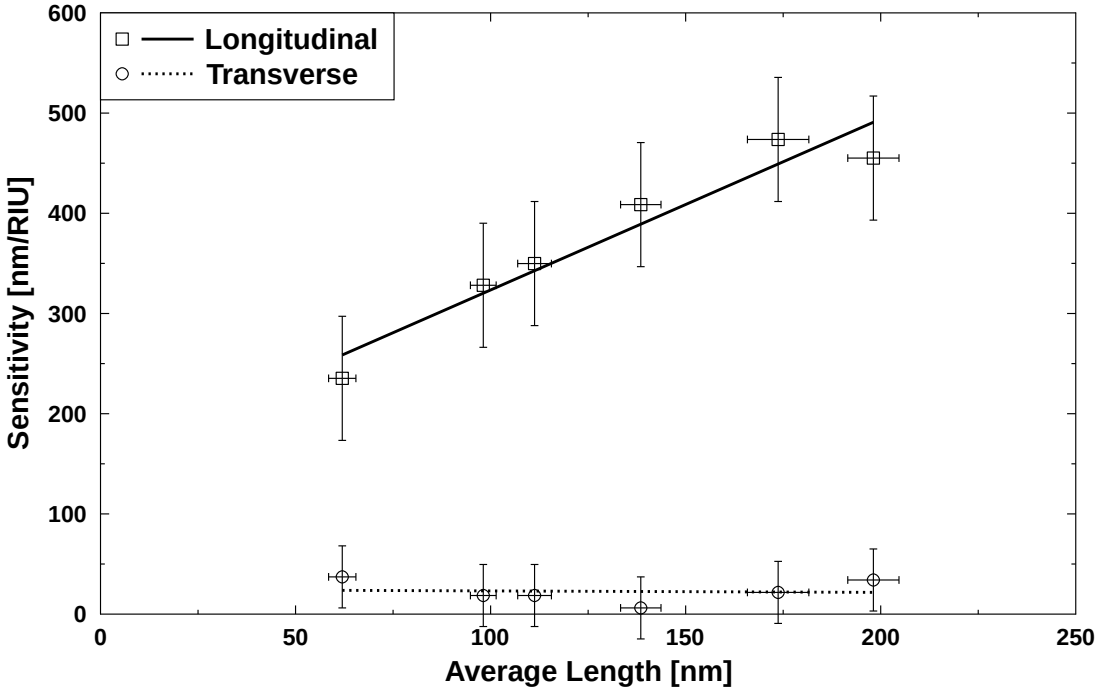

Figure 4.15: Refractive index sensitivity of gold slanted post samples of different average lengths. The sensitivity is the wavelength shift in nanometres per refractive index unit (RIU).

4.5 Phi-Sweep Films

Although the initial goal was to investigate the use of phi-sweep GLAD films for LSPR biosensing, the use of phi-sweep films was abandoned in favour of using spherical particle films, grown by constant film rotation during the deposition. This was due to the sharper extinction peaks of the spherical particle films as compared to the slanted post films and phi-sweep films. In addition, the isotropic nature of the spherical particle films simplified the optical measurements. Finally, the slanted post films being used were quite thin (less than 200 nm thick), and as such, the effects of broadening and fanning were not present to a large degree, as can be seen in the SEM image in Fig. 4.16a of a 50 nm thick gold slanted post film grown at a deposition angle of 86°. An image of a 50 nm thick gold phi-sweep film that was grown with a deposition angle of 86°, a sweep angle of 30°, and a sweep pitch of 5 nm is shown in Fig. 4.16b for comparison. There still appears to be some slight broadening of the columns in the phi-sweep film. This could be due to the relatively small sweep pitch of 5 nm being non-optimal for reducing broadening. A similar broadening effect using low sweep pitch was reported by Jensen and Brett for silicon films [65]. Since the main purpose of the phi-sweep technique is to prevent broadening and fanning effects in slanted post films, there was no perceived benefit to using phi-sweep for this application.

An interesting effect of the phi-sweep technique can be seen in the extinction spectra in Fig. 4.17. The extinction peak of the phi-sweep film in the transverse mode is red-shifted by 5 nm to a peak at 542 nm compared to the traditional GLAD film at 537 nm, while the peak of the phi-sweep film in the longitudinal mode is blue-shifted by 37 nm to a peak at 660 nm compared to the traditional GLAD film at 697 nm. The separation between the resonance peaks of the transverse and longitudinal modes for the phi-sweep film is 118 nm, which is less than the separation of 160 nm for the traditional GLAD film. This could be caused by the fact that the phi-sweep technique causes the tilt angle between the post axis and the substrate normal to be less than that of a traditional GLAD film grown at the same deposition angle, as described earlier in Chapter 3. This would cause a phi-sweep film to present a more circular cross-section to the incident light, which arrives along the substrate normal, than a traditional GLAD film, effectively decreasing its χ value.

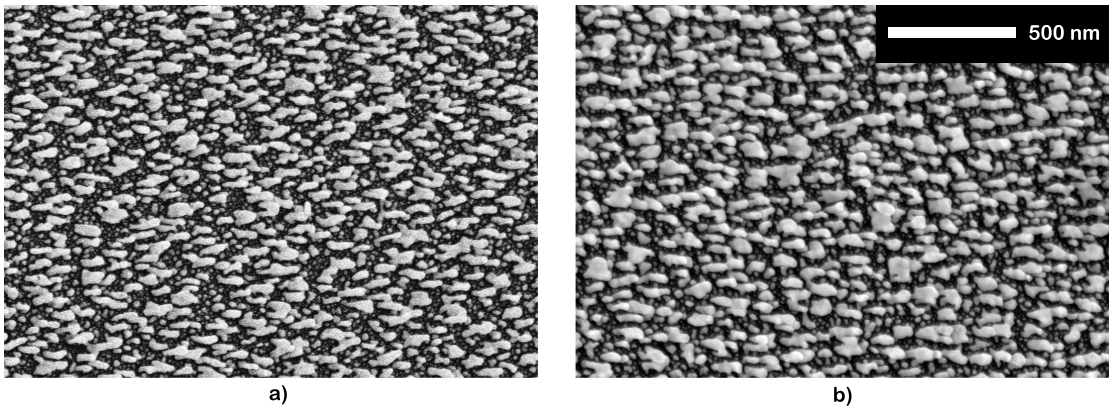

Figure 4.16: Scanning electron microscopy images of a 50 nm thick gold slanted post film grown using (a) traditional GLAD, and (b) phi-sweep.

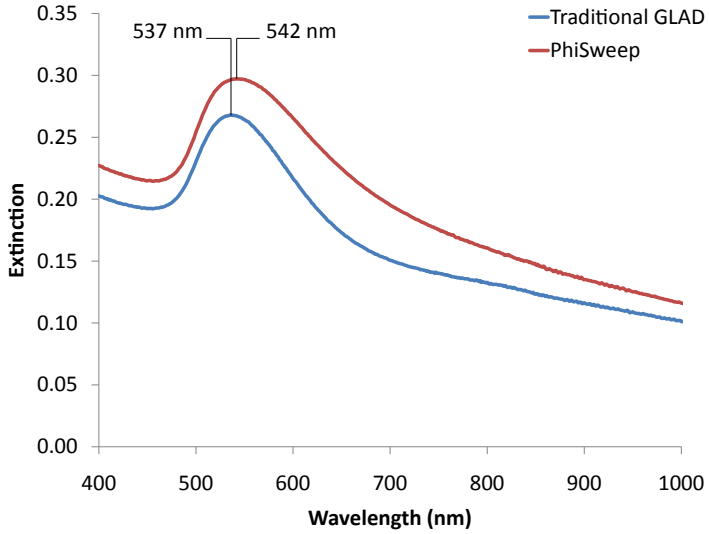

(a)

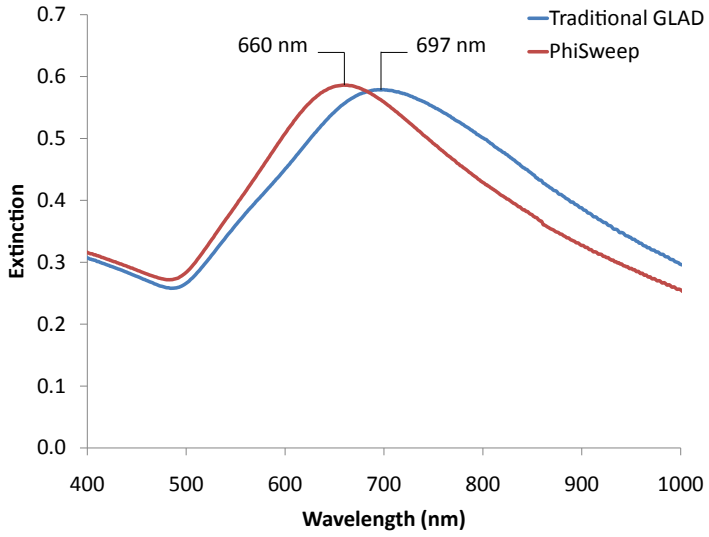

(b)

Figure 4.17: Extinction spectra of both a 50 nm thick traditional GLAD slanted post film and a 50 nm thick phi-sweep film for both the a) transverse and b) longitudinal polarizations.

4.6 Ageing Effects

To investigate how ageing affects the optical properties of noble metal GLAD films, the optical properties of spherical gold particle samples were measured several times over a period of two weeks. The samples were deposited on glass substrates at a deposition angle of 86°, and were grown to a thickness of approximately 20 nm. An SEM image of a typical sample is shown in Fig. 4.18a. The samples were stored in a petri dish in laboratory air over the course of the study. The extinction spectra over the two week period are shown in Fig. 4.18b. The times displayed in the figure are elapsed times from the moment the samples were removed from the deposition chamber.

The extinction peak red-shifted and the maximum extinction increased in value over the two week period. Figs. 4.19a and 4.19b show the change in peak extinction and peak wavelength for two samples. This suggests that the refractive index near the gold surface is increasing over time. This is likely due to the accumulation of contaminants from the air on the gold surface. The contaminants may have included volatile organics from the plastic petri dish. It is possible that humidity could also cause shifts in the peak position, as any water molecules adsorbed to the metal surface would increase the local refractive index. Since silver is more reactive than gold, it is likely that these ageing effects would be more pronounced in silver films. One group reported a 65 nm red-shift in the resonant peak wavelength in 36 h for samples of 60 nm diameter silver particle arrays stored in laboratory air, which was attributed to sulfur contamination [92]. This suggests that long term storage would be an important concern for any application of these films and would require special consideration.

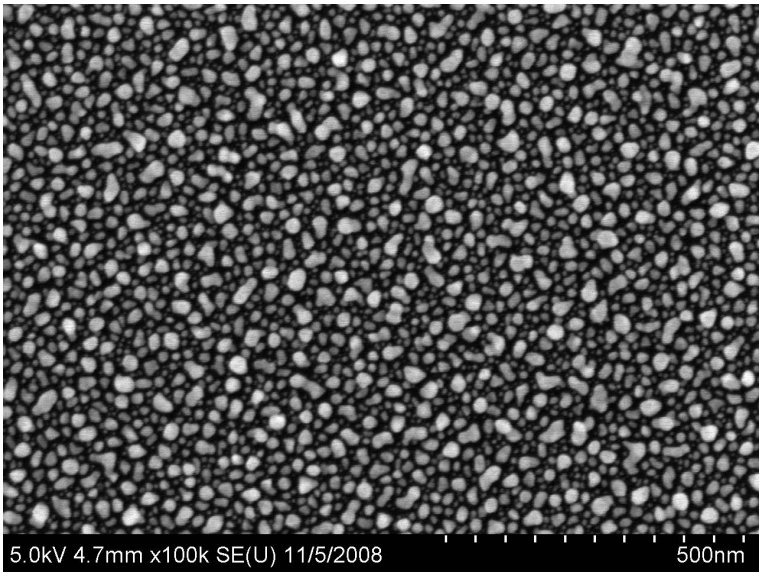

(a)

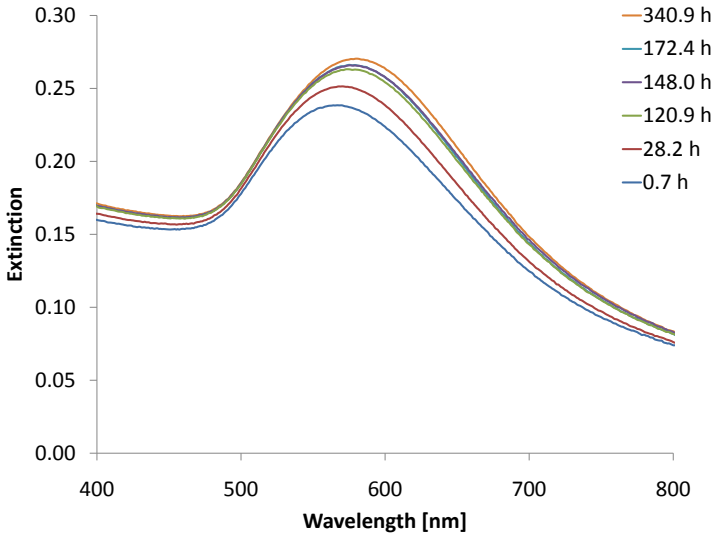

(b)

Figure 4.18: a) SEM image of a 20 nm thick spherical gold film and b) extinction spectra of the film over a two week period. Time shown is time elapsed from removal from the deposition chamber.

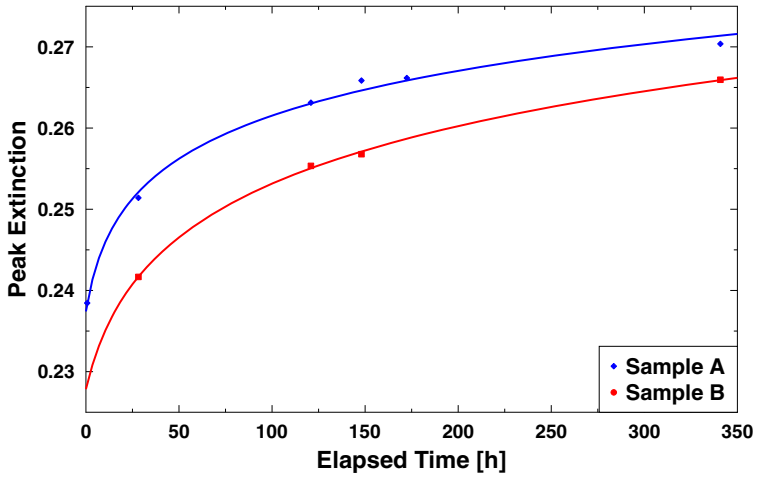

(a)

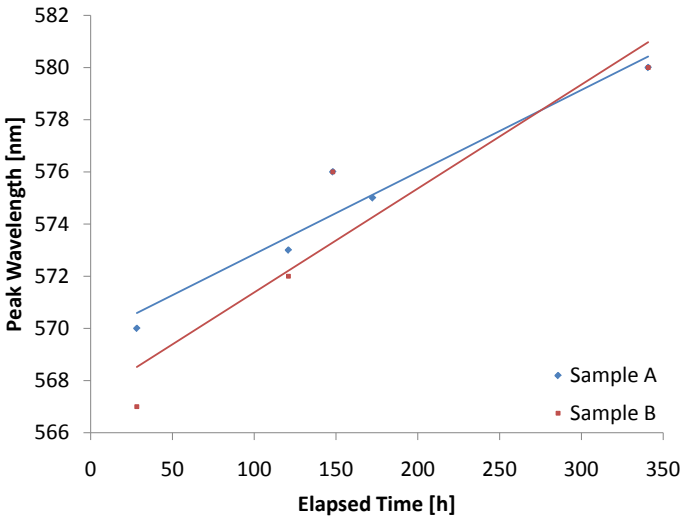

(b)

Figure 4.19: Change in a) peak extinction and b) peak wavelength of a 20 nm thick spherical gold film over a two week period. Time shown is time elapsed from removal from the deposition chamber. The curves are a guide to the eye.

5 LSPR BIOSENSING WITH GLAD FILMS[1]

5.1 Introduction

A common biochemical test is an immunoassay, which measures the concentration of a substance in a biological liquid by using the reaction of an antibody to its antigen. The binding between an antibody and its antigen is both strong and specific, and has been widely exploited for sensor design [94]. Immunoassays can be used to detect the presence of the antigen or the antibody. Typical immunoassays involve immobilizing either the antigen or the antibody to a surface to use as a recognition layer and then detecting the binding of the partner molecule [94]. The LSPR biosensing capability of silver nanoparticle films fabricated by GLAD was evaluated by detecting the binding of anti-rabbit immunoglobulin G (anti-rIgG) to a rabbit immunoglobulin G (rIgG) recognition layer on the nanoparticle surface. Here rIgG is acting as the antigen, and its antibody is anti-rIgG. The research in this chapter was done in collaboration with M. T. McDermott et al.

5.2 Experimental Procedure

Silver nanoparticles were fabricated by glancing angle deposition using an electron beam evaporation system. Prior to deposition, $1'' \times 1''$ fused silica substrates were cleaned using Citranox cleaner from Alconox, Inc. (White Plains, New York). The substrates were loaded on a motor controlled substrate holder located 42 cm above the electron beam crucible. The vapour source material was silver shot from Cerac (Milwaukee, Wisconsin) with a purity of 99.99%. The chamber was evacuated to a base pressure of 1.5×10^{-5} Pa by cryogenic pumping. Deposition of the silver was carried out at a pressure of 1.3×10^{-4} Pa.

The substrates were held at an oblique angle, α, of 85°, while ϕ was constantly rotated at a rate of one revolution for every 3 nm of film growth. The deposition rate was measured by a quartz crystal microbalance (QCM) and was kept at 1 Å/s. The the film was grown

[1] A version of this chapter has been published in Ref. [93].

to a thickness of approximately 150 nm. After film growth, top down and cross-sectional images of the film were obtained by scanning electron microscopy (SEM). The samples were stored in a nitrogen environment.

5.2.1 Extinction Measurements

Extinction measurements of the samples were taken using a PerkinElmer Lambda 900 UV/VIS/NIR spectrophotometer with a resolution of 1 nm. For measurements in solvents, the samples were cleaved and placed in a 3.5 mL glass cuvette that was filled with the desired liquid. All of the spectra measurements were performed in standard transmission geometry with unpolarized light.

The stability of the films' optical properties after being immersed in solvents was investigated using two methods. First, the extinction spectrum of an as deposited film was measured in air. The sample was then immersed in liquid for a total of 4 hours, and taken out every hour to measure the extinction spectrum. Before each measurement, the sample was dried under nitrogen flow, and the measurement was taken with the sample in air. The liquid used alternated every hour between methanol and deionized water, starting with methanol. For the second method, the extinction spectrum of a sample was taken before and after the sample had soaked in deionized water for 24 hours. After the 24 hour soaking period, the sample was dried under nitrogen flow and the measurement was taken with the sample in air. In order to stabilize the intensity of the extinction spectra, all other samples in this study were first allowed to soak in deionized water for 24 hours before being used for subsequent measurements or functionalization steps.

To evaluate the sensitivity of the films to changes in the refractive index of their environment, extinction spectra of a sample were measured while immersed in liquids of various refractive indices. The liquids used were deionized water, 2-propanol, and chloroform with refractive indices of 1.33, 1.38, and 1.45, respectively. After each measurement, the sample was dried under nitrogen flow and the extinction spectrum was measured in air before the sample was immersed in a different liquid.

Noise Equivalent Extinction

To investigate the PerkinElmer instrument's capability for accurate measurement of the extinction spectra, the noise equivalent extinction for a typical sample was measured.

The noise equivalent extinction, $E_{noise}(\lambda)$ is defined as:

$$E_{noise}(\lambda) = -\log(T_{noise}(\lambda)) \tag{5.1}$$

where $T_{noise}(\lambda)$ can be found by measuring the transmittance of the same sample several times and taking the standard deviation of the values at each wavelength.

The transmittance spectra of a typical sample was measured 5 times in a row over the course of 1 hour. This data was used to find $T_{noise}(\lambda)$, and from it $E_{noise}(\lambda)$ was calculated using Eq. 5.1. The resulting noise equivalent extinction spectrum, along with one of the five transmittance spectra (converted to extinction for comparison) is shown in Fig. 5.1.

The higher the noise equivalent extinction, the less noise is in the data. A larger difference between the noise equivalent extinction and the sample extinction leads to a higher signal-to-noise ratio. At its worse, the noise equivalent extinction is almost a full unit higher than the sample extinction. This translates to a transmittance signal-to-noise ratio of nearly 10. This occurs at the resonance peak, the wavelength where the most amount of light is getting absorbed and scattered by the sample. This is an acceptable noise equivalent extinction to be confident in the measurement.

5.2.2 Biosensor Preparation and Testing

Prior to biosensor preparation, the extinction spectrum of the sample was measured. The sample was then soaked overnight in 2 mM 11-Amino-1-undecanethiol (11-AUT) in water from Dojindo Laboratories (Japan). The extinction spectrum was measured again after the sample was rinsed in deionized water and dried under nitrogen flow. Next the sample was immersed in 6.7 μM rIgG in 1 mM phosphate buffered saline (PBS), pH=7.4, for 1 hour. Following this, the sample was first rinsed with 1 mM PBS to wash away unbound proteins, and then deionized water to prevent salt deposits from forming. Finally, the sample was dried under nitrogen flow before taking another extinction spectrum measurement.

To test the biosensor, a sample which was functionalized with 11-AUT and rIgG was immersed in varying concentrations of polyclonal (goat) anti-rIgG. Each immersion lasted for 1 hour and proceeded from the lowest concentration of 13 nM up to a maximum concentration of 6.7 μM. The sample's extinction spectrum was measured following each immersion after it was rinsed in PBS and deionized water, and dried under nitrogen flow.

To ensure that the binding between rIgG and 11-AUT is stable, a second functionalized

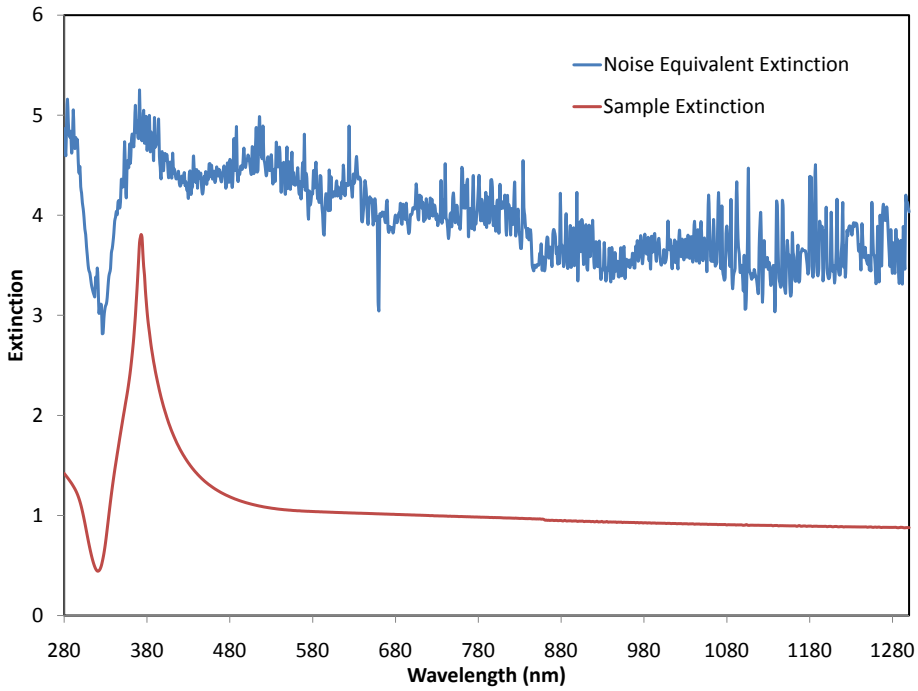

Figure 5.1: Noise equivalent extinction for a typical sample. One of the extinction spectra used to calculate the noise equivalent extinction is also shown.

sample was immersed in 1 mM PBS solution for 1 hour, and an extinction spectrum was measured after the sample was rinsed and dried. This same sample was then immersed in 1.06 μM polyclonal (rabbit) anti-goat immunoglobulin G (anti-gIgG) for 1 hour to investigate the selectivity of the sensor. An extinction spectrum was measured after the sample was rinsed and dried. Finally, the sample was placed in a 1.06 μM solution of anti-rIgG for 1 hour to ensure that the sample was still sensitive to anti-rIgG. The sample was rinsed and dried before an extinction measurement was taken.

All of the immunoglobulin solutions used in this study were obtained from MP Biomedicals, LLC. (Solon, Ohio). The biosensor extinction measurements were taken with the sample in air.

5.3 Results and Discussion

The structure of the films was observed by scanning electron microscopy (SEM). A typical top-view image of the Ag nanostructures is shown in Fig. 5.2a. The image shows a dense collection of silver nanoparticles, the majority of which are spherical and have diameters ranging from approximately 20 to 300 nm. The thickness of the film, defined as the average height of the dominant features, was measured from the cross-sectional SEM image shown in Fig. 5.2b, and was found to be approximately 150 nm.

The GLAD technique allows silver nanoparticle films to be fabricated in a one-step deposition process. Although LSPR studies have been done using ultrathin silver and gold island films evaporated or sputtered at normal incidence [68, 69, 72, 74, 95, 96], the GLAD technique allows for the density of the film to be easily controlled by adjusting the deposition angle, α. Also, the maximum film thickness is not limited by island aggregation and coalescence due to the self shadowing effect during GLAD film growth. Finally, the shape of Ag nanoparticles produced by GLAD is not limited to spheres. Other groups using the GLAD technique or oblique angle deposition have demonstrated the growth of prolate silver nanoparticles and tilted silver nanorod arrays with polarized optical absorbance and surface enhanced Raman spectra [73, 80, 81, 97, 98, 99]. For this initial study on LSPR biosensors using GLAD, a simple vertical column structure was used. However, more complex structures that may provide enhanced biosensor performance are currently under investigation.

The UV-visible extinction spectrum of the as deposited silver films exhibits a strong

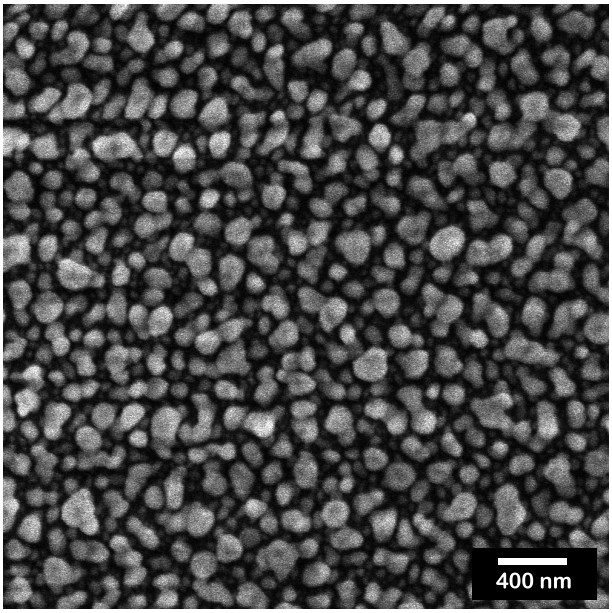

(a)

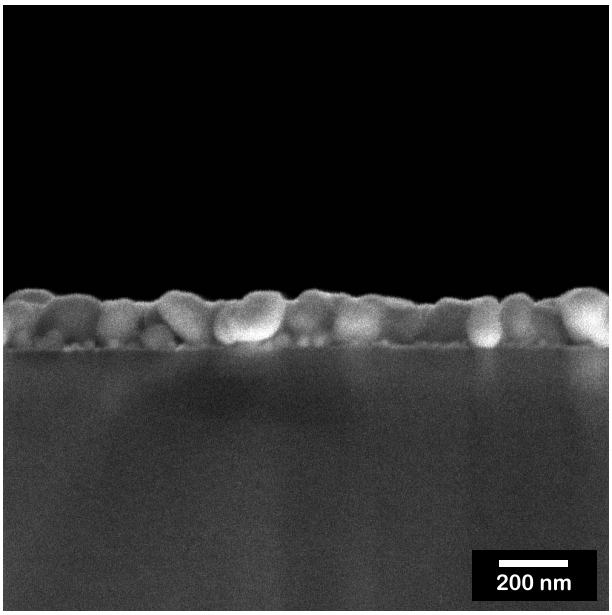

(b)

Figure 5.2: Scanning electron microscopy images of (a) the top surface, and (b) the cross-section of the Ag nanoparticle film on a fused silica substrate.

peak around a wavelength of 368 nm in air due to the LSPR, as shown in Fig. 5.3a. For biosensing use, the samples should be stable when immersed in solvents. The stability of the films was examined by immersing a sample in alternating solutions of methanol and deionized water for 1 hour increments and observing any changes in their extinction spectra. As shown in Fig. 5.3a, while the position of the extinction peak is quite stable, with a maximum peak shift of less than ±2 nm from the as deposited value, the intensity of the peak decreases after each hour in solution. The amount of the peak extinction decreases are 0.38, 0.17, 0.07, and 0.04 after the 1st, 2nd, 3rd, and 4th hour measurements, respectively. The stability of the peak position implies that the general shape of the particles is not significantly affected by the solvents. This is in contrast to previous work where large peak shifts of around 100 nm and particle shape changes are observed following "solvent annealing" [70]. The stability of the peak position is most important in this study since it is this parameter that will be used to detect changes in the refractive index surrounding the silver particles. The intensity decreases observed here are likely due to a loss of some of the silver material from the substrate perhaps via dissolution. The sample that was immersed in deionized water for 24 hours behaved similarly, with a peak shift of -2 nm from its as deposited position, but with a greater reduction in peak extinction of 1.0. However, since the magnitude of intensity change decreases after every hour in solution, the extinction intensity is somewhat stabilized for longer soaking times. Therefore, all the remaining samples used in this study were first allowed to soak in deionized water for 24 hours before being used for subsequent measurements or functionalization steps.

To investigate the dependence of the LSPR peak extinction wavelength on the refractive index of the surrounding medium, the extinction spectra were measured while a sample was immersed in liquids with varying refractive indices. The liquids used were deionized water, 2-propanol, and chloroform, with refractive indices of 1.33, 1.38, and 1.45, respectively. The wavelength shift of the extinction peak was found to be linearly dependent on the refractive index, with a wavelength shift per refractive index unit (RIU), or sensitivity factor, of 123 ± 3 nm/RIU and an R^2 value of 0.9998. This linear dependence has been reported by many groups and the sensitivity factor is comparable to reported values [8, 77, 78, 79]. After each measurement in solution, the sample was dried and a measurement was made with the sample in air to ensure the peak position returned to its initial value. The peak position consistently returned to within 2 nm of the initial spectrum peak, while the peak intensity decreased only slightly after all the measurements in

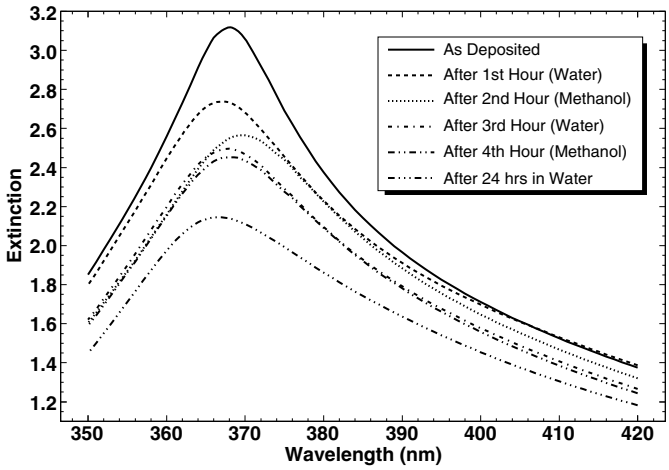

(a)

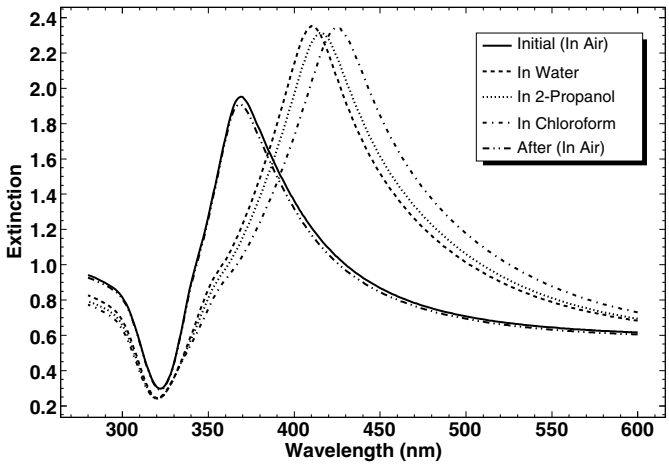

(b)

Figure 5.3: (a) Extinction spectra in air of an as deposited film, and after being immersed in solvents for various time periods. (b) Extinction spectra in air before solvent measurements, in solvents of varying index of refraction, and in air again after the solvent measurements. The refractive index of each solvent is 1.33, 1.38, and 1.45 for water, 2-propanol, and chloroform, respectively.

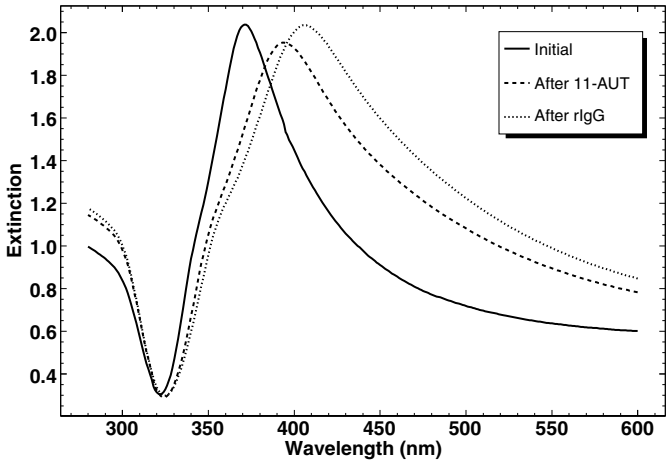

Figure 5.4: The initial extinction curve before sample functionalization, and extinction curves after the 11-AUT and rIgG functionalization steps.

solution were complete. The initial spectrum in air, the extinction spectra in the different solutions, and the spectrum in air after the solution measurements are shown in Fig. 5.3b.

The refractive index dependence of the LSPR extinction peak can be used to detect the binding of biomolecules to the silver nanoparticles' surface, since the biomolecule adsorption causes an increase in the local refractive index. In this study, the binding event between rIgG and anti-rIgG is detected. To prepare the biosensors, the films were first functionalized with a self assembled monolayer of 11-AUT. Rabbit immunoglobulin G was then immobilized to the sensor by non-specific adsorption to the amino group of the 11-AUT. The extinction spectra of a sample film before modification and after each functionalization step is shown in Fig. 5.4. The peak extinction wavelength of the film before modification is 371 nm. After modification with 11-AUT and rIgG, the peak red-shifted to 393 nm and 406 nm, respectively. This corresponds to a red-shift of 22 nm after 11-AUT modification, and a further 13 nm red-shift after rIgG binding. The reproducibility of the shift after AUT and rIgG modification with three samples is a standard deviation of ± 3 nm.

After the film is functionalized with rIgG, it can detect the binding of anti-rIgG. An antibody capture binding curve was measured to test the sensor's functionality. The sensor was exposed to different concentrations of anti-rIgG and the resulting peak wavelength shift was measured. Figure 5.5a shows a selection of the spectra that were collected, while

Fig. 5.5b shows the peak wavelength shift, $\Delta\lambda$, versus anti-rIgG concentration, [anti-rIgG], fit with the Langmuir isotherm:

$$\Delta\lambda = \Delta\lambda_{max} \frac{K_a\,[\text{anti-rIgG}]}{1 + K_a\,[\text{anti-rIgG}]} \tag{5.2}$$

where $\Delta\lambda_{max}$ is the saturation value of the extinction peak wavelength shift, and K_a is the surface-confined thermodynamic affinity constant. The wavelength shift was calculated in reference to the peak wavelength after the sample was functionalized with 11-AUT and rIgG. The saturation value, $\Delta\lambda_{max}$, and the affinity constant, K_a, were used as fit parameters, and were determined to be $\Delta\lambda_{max} = 29.4 \pm 0.7$ nm and $K_a = (2.7 \pm 0.3) \times 10^6$ M^{-1} by the minimization by a gradient (MIGRAD) method provided by the ROOT data analysis package [100]. The peak wavelength shift at a concentration of 6.7 μM is 28 $\pm$ 1 nm, which is close to the calculated saturation value. The K_a value determined here is comparable to that determined for similar IgGs with SPR imaging [94]. With respect to detection limit, we estimate that the minimum wavelength shift observable is approximately 2 nm. From the data collected in Fig. 5.5b, this corresponds to 27 nM of the antibody. We expect improved detection limits with optimized film structures.

To ensure the binding of rIgG to 11-AUT is stable, a sample that was functionalized with 11-AUT and rIgG was soaked in 1 mM PBS for 1 hour, and a spectrum was measured after rinsing and drying the sample. The peak position was quite stable and blue-shifted by less than 1 nm. To test the response of the films to non-specific binding, the same sample was exposed to a 1.06 μM solution of anti-goat IgG for 1 hour. This resulted in a peak wavelength shift of about +1 nm. Finally, the sample was soaked in 1.06 μM of anti-rIgG for 1 hour to verify that the biosensor surface remained active after anti-gIgG exposure. This resulted in a peak shift of +17 nm. Thus, the sensor is responding to the specific binding between anti-rIgG and rIgG with a limited response to non-specific binding. The response of the sample to anti-rIgG was slightly less than the expected value of 22 nm from the fit to the data in Fig. 5.5b, which indicates a slight loss in sensitivity after exposure to the PBS and anti-gIgG solutions. Figure 5.6 shows the extinction spectra of the functionalized sample before and after exposures to the 1 mM PBS, 1.06 μM anti-gIgG and 1.06 μM anti-rIgG.

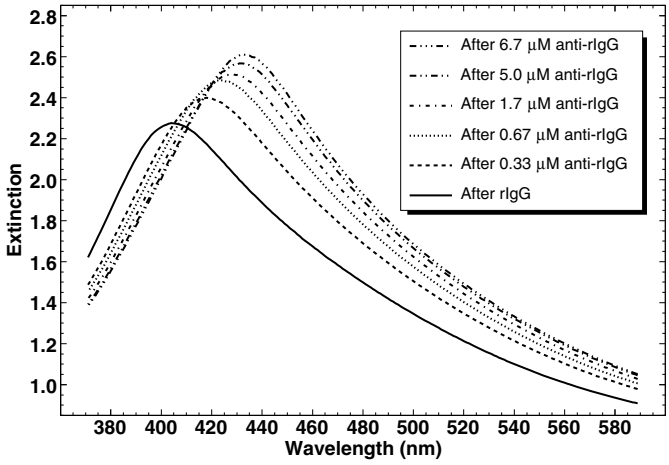

(a)

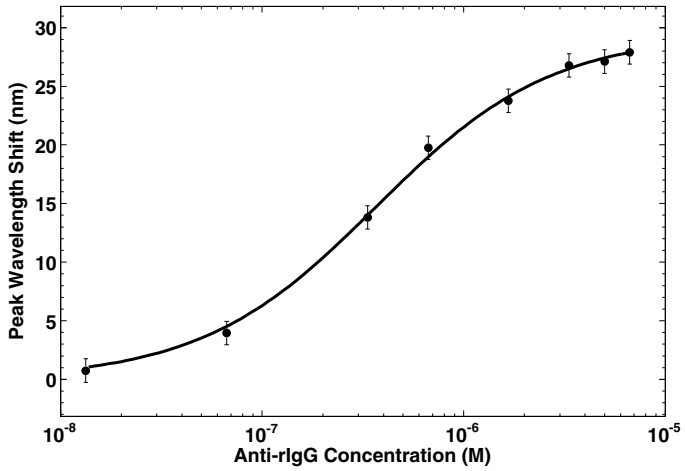

(b)

Figure 5.5: (a) Extinction spectrum of rIgG functionalized sample, and a selection of the extinction spectra after exposure to solutions of varying concentrations of anti-rIgG. (b) Peak LSPR extinction wavelength shift as a function of anti-rIgG concentration. The curve is a fit to the Langmuir isotherm given in Eq. 5.2. The error bars are estimates of the uncertainty in the wavelength shifts.

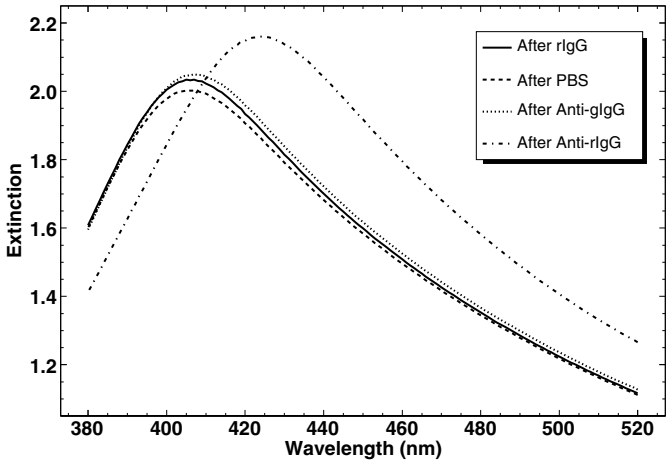

Figure 5.6: Extinction spectrum of rIgG functionalized sample, and spectra after incubation in 1 mM PBS, 1.06 μM anti-gIgG, and 1.06 μM anti-rIgG.

5.4 Conclusion

Silver nanostructured films were fabricated by glancing angle deposition for use as localized surface plasmon resonance biosensors. The films exhibited an LSPR extinction peak which was observed to red-shift linearly with increasing refractive index of the surrounding medium. The sensitivity factor was found to be 123 nm/RIU. Evaluation of the samples as LSPR biosensors was performed by functionalizing the surface with 11-AUT and rIgG, which allowed for the detection of anti-rIgG binding. The binding data was fit to the Langmuir isotherm, which yielded values for the saturation value of the wavelength shift, $\Delta\lambda_{max} = 29.4 \pm 0.7$ nm, and the surface confined thermodynamic binding constant, $K_a = (2.7 \pm 0.3) \times 10^6$ M^{-1}. Also, the response to non-specific binding was investigated by exposing a functionalized film to 1.06 μM anti-goat IgG, which resulted in a peak wavelength shift of approximately 1 nm. This study has demonstrated the feasibility of using silver nanoparticle films fabricated by GLAD for LSPR based biosensing. The advantages of GLAD include the ability to produce large area silver nanoparticle films in a one-step deposition process at low cost, without the nanoparticle size being limited by island aggregation and coalescence. However, improvements to the sensor properties are needed. The ability to control the film density and nanoparticle shape by the GLAD process may allow for the optimization of these properties.

6 CONCLUSION

6.1 Summary of Research Results

In the field of nano and microfabrication, gaining additional control over the morphology of the resulting structures is a major benefit. For instance, the morphology of the individual columns in a GLAD film plays an integral part in determining the properties of the engineered film as a whole, including the optical, mechanical, and electrical properties. Being able to manipulate and customize these properties is of great interest when developing applications of a technology such as GLAD.

In this thesis, an enhancement to GLAD technology called phi-sweep was investigated. The phi-sweep technique was used to grow silicon and TiO_2 slanted column structures on substrates pre-patterned with square lattice arrays of substrate seeds. Column fanning was shown to be significantly reduced compared to slanted columns grown by traditional GLAD on identical substrates. The tilt angle, β, of the slanted columns was predicted to be modified by the phi-sweep technique according to $\tan(\beta_{PS}) = \tan(\beta_{TG})\cos(\gamma)$, where γ is the sweep angle. This dependence was derived from geometrical arguments and tested experimentally. The results of the experiment showed the model to be valid, and has led to a better understanding of the phi-sweep technique.

When developing a technology, the main motivation is for the technology to be useful for some application. Since the beginning of its development, GLAD has been studied and used in numerous applications, with new ones being continually developed. In this thesis, GLAD technology has been used to fabricate biosensors based on localized surface plasmon resonance in metallic nanostructures. Films of silver and gold nanoparticles were fabricated on fused silica substrates using GLAD. The localized surface plasmon resonant wavelength was determined by measuring the extinction spectra of the samples. Initial experiments explored the effect of placing the samples in different media, and it was found that the resonant wavelength was linearly dependent on the refractive index of the medium.

Two morphologies of metallic structures were investigated: spherical particles and

slanted columns. The spherical particles had one main peak in the extinction spectrum. However, due to the anisotropic nature of the slanted column films, these samples had two extinction peaks at different wavelengths. These different peaks corresponded to the longitudinal and transverse modes of localized surface plasmon resonance. The longitudinal mode was caused by excitation along the long axis of the column, while the transverse mode was due to excitation along the short axis. The extinction peak due to the longitudinal mode was red-shifted relative to the peak caused by the transverse mode. The separation between the two peaks increased for longer columns. The resonant wavelength of the longitudinal mode was found to be much more sensitive to the surrounding refractive index than the transverse mode. In addition, the sensitivity of the longitudinal mode generally increased with column length. Since the slanted columns were aligned, the different modes could be selectively excited with the use of linear polarizing optics.

The effects of sample aging were investigated by taking measurements of the extinction spectra of gold spherical particle samples over a two-week period. The samples' extinction peaks increased in magnitude and red-shifted during the measurement period, indicating that the samples' surface were being contaminated while stored in ambient laboratory air. This has repercussions for any application of these films that would require long-term storage of the devices before use. Perhaps by sealing the devices in proper packaging, contamination could be delayed or avoided.

The dependence of the resonant wavelength on the refractive index of the medium surrounding the metallic particles was exploited to detect the binding of biomolecules to the metal surface. The surface of silver spherical particle films were functionalized with an 11-Amino-1-undecanethiol adhesion layer and a rabbit immunoglobulin G recognition layer to allow for the selective detection of anti-rabbit immunoglobulin G molecules. The extinction peak red-shifted a distance dependent on the concentration of anti-rIgG solution in a manner described by the Langmuir isotherm with a saturation value, $\Delta\lambda_{max}$, of 29.4 ± 0.7 nm and a surface confined thermodynamic binding constant, K_a, of $(2.7 \pm 0.3) \times 10^6$ M^{-1}. The limit of detection was determined to be 27 nM.

6.2 Suggested Future Work

It would be of interest to evaluate other film morphologies for LSPR biosensing. However, since silver and gold have relatively low melting points, it is difficult to engineer GLAD

films with more complex morphologies, such as chevrons or helices, using these materials. It is hypothesized that cooling the substrate during the deposition would reduce the mobility of the silver or gold adatoms, causing the material to better conform to the desired morphology. Work on cooled substrates is already in progress by my colleagues in the GLAD Laboratory at the University of Alberta, showing promising results in reducing diffusivity and achieving more isolated columns.

Another improvement to LSPR sensors would be to improve the uniformity of the particles' shape, size and relative position. This would lead to sharper extinction peaks, which allow for more precise measurements of the peak wavelength. Greater uniformity could be achieved using pre-patterned substrates to "seed" areas on top of which particles could begin to grow. However, this would introduce extra fabrication steps and processing that are necessary to produce the patterned substrate topography. In addition, it is desirable to achieve good structural uniformity over reasonable substrate areas if this technology is to be commercialized. This would rule out any direct-write methods such as electron-beam lithography or laser direct-write lithography, as creating large patterned areas with these techniques is slow and costly.

6.3 Final Remarks

This thesis has both improved the understanding of the phi-sweep technique, and developed biosensors based on localized surface plasmon resonance of noble metal GLAD films. While more work needs to be done if GLAD LSPR biosensors are ever to become useful devices, significant progress has been made towards this end.

REFERENCES

[1] J. Fujita, Y. Ohnishi, Y. Ochiai, and S. Matsui, "Ultrahigh resolution of calixarene negative resist in electron beam lithography," *Applied Physics Letters* **68**, 1297–1299 (1996). (Cited on page 1.)

[2] P. Thomas, G. Kulkarni, and C. Rao, "Dip-pen lithography using aqueous metal nanocrystal dispersions," *Journal of Materials Chemistry* **14**, 625–628 (2004). (Cited on page 1.)

[3] L. Guo, "Recent progress in nanoimprint technology and its applications," *Journal of Physics D-Applied Physics* **37**, R123–R141 (2004). (Cited on page 1.)

[4] E. Thostenson, Z. Ren, and T. Chou, "Advances in the science and technology of carbon nanotubes and their composites: a review," *Composites Science and Technology* **61**, 1899–1912 (2001). (Cited on page 2.)

[5] Y. Feng, W. Teo, K. Siow, Z. Gao, K. Tan, and A. Hsieh, "Corrosion protection of copper by a self-assembled monolayer of alkanethiol," *Journal of the Electrochemical Society* **144**, 55–64 (1997). (Cited on page 2.)

[6] I. Hamley, "Nanostructure fabrication using block copolymers," *Nanotechnology* **14**, R39–R54 (2003). (Cited on page 2.)

[7] P. Ball, "It all falls into place...," *Nature* **413**, 667–668 (2001). (Cited on page 2.)

[8] T. Jensen, M. Duval, K. Kelly, A. Lazarides, G. Schatz, and R. Van Duyne, "Nanosphere lithography: Effect of the external dielectric medium on the surface plasmon resonance spectrum of a periodic array of sliver nanoparticles," *Journal of Physical Chemistry B* **103**, 9846–9853 (1999). (Cited on pages 2 and 59.)

[9] L. Canham, "Silicon quantum wire array fabrication by electrochemical and chemical dissolution of wafers," *Applied Physics Letters* **57**, 1046–1048 (1990). (Cited on page 2.)

[10] H. Foll, M. Christophersen, J. Carstensen, and G. Hasse, "Formation and application of porous silicon," *Materials Science & Engineering R-Reports* **39**, 93–141 (2002). (Cited on page 2.)

[11] J. C. Sit, D. Vick, K. Robbie, and M. J. Brett, "Thin film microstructure control using glancing angle deposition by sputtering," *Journal of Materials Research* **14**, 1197–1199 (1998). (Cited on page 5.)

[12] D. Vick, Y. Y. Tsui, M. J. Brett, and R. Fedosejevs, "Production of porous carbon thin films by pulsed laser deposition," *Thin Solid Films* **350**, 49–52 (1999). (Cited on page 5.)

[13] A. Kundt, "Ueber doppelbrechung des lichtes in metallschichten, welche durch zerstäuben einer kathode hergestellt sind," *Annalen der Physik und Chemie* **263**, 59–71 (1886). (Cited on page 5.)

[14] F. Kaempf, "Size and reasons for the double refraction and artificial mirrors and origin of double refraction in metals," *Annalen der Physik* **16**, 308–333 (1905). (Cited on page 5.)

[15] C. Maurain, "Dichroism, birefringence and conductibility of thin metallic laminas obtained by cathodic pulverisation.," *Comptes Rendus Hébdomadaires des Séances de l'Academie des Sciences* **142**, 870–872 (1906). (Cited on page 5.)

[16] C. Bergholm, "The double break in cathode atomised metal layers, (Preliminary announcement)," *Annalen der Physik* **43**, 1–23 (1913). (Cited on page 5.)

[17] T. G. Knorr and R. W. Hoffmann, "Dependence of geometric magnetic anisotropy in thin iron films," *Physical Review* **113**, 1039–1046 (1959). (Cited on page 5.)

[18] D. O. Smith, "Anisotropy in permalloy films," *Journal of Applied Physics* **30**, 264S–265S (1959). (Cited on page 5.)

[19] M. S. Cohen, "Anisotropy in permalloy films evaporated at grazing incidence," *Journal of Applied Physics* **32**, 87S–88S (1961). (Cited on page 5.)

[20] H. Konig and G. Helwig, "*Uber die struktur schrag aufgedampfter schichten und ihr einfluss auf die entwicklung submikroskopischer oberflachenrauhigkeiten," *Optik* **6**, 111–124 (1950). (Cited on page 5.)

[21] D. O. Smith, M. S. Cohen, and G. P. Weiss, "Oblique-incidence anisotropy in evaporated permalloy films," *Journal of Applied Physics* **31**, 1755–1762 (1960). (Cited on page 5.)

[22] R. Tait, T. Smy, and M. Brett, "Modeling and characterization of columnar growth in evaporated-films," *Thin Solid Films* **226**, 196–201 (1993). (Cited on pages 6 and 18.)

[23] S. Dew, "Theoretical and practical aspects of collimated sputtering," *Journal of Applied Physics* **76**, 4857–4862 (1994). (Cited on page 7.)

[24] M. Malac, R. F. Egerton, M. J. Brett, and B. Dick, "Fabrication of submicrometer regular arrays of pillars and helices," *Journal of Vacuum Science & Technology B: Microelectronics and Nanometer Structures* **17**, 2671–2674 (1999). (Cited on page 7.)

[25] B. Dick, M. J. Brett, and T. Smy, "Controlled growth of periodic pillars by glancing angle deposition," *Journal of Vacuum Science & Technology B: Microelectronics and Nanometer Structures* **21**, 23–28 (2003). (Cited on page 7.)

[26] M. O. Jensen and M. J. Brett, "Periodically structured glancing angle deposition thin films," *IEEE Transactions on Nanotechnology* **4**, 269–277 (2005). (Cited on page 7.)

[27] S. V. Kesapragada and D. Gall, "Two-component nanopillar arrays grown by glancing angle deposition," *Thin Solid Films* **494**, 234–239 (2006). (Cited on page 7.)

[28] S. Kennedy, M. Brett, O. Toader, and S. John, "Fabrication of tetragonal square spiral photonic crystals," *Nano Letters* **2**, 59–62 (2002). (Cited on pages 7, 11, and 12.)

[29] N. Young and J. Kowal, "Optically active fluorite films," *Nature* **183**, 104–105 (1959). (Cited on page 7.)

[30] K. Robbie, M. Brett, and A. Lakhtakia, "Chiral sculptured thin films," *Nature* **384**, 616 (1996). (Cited on pages 7 and 10.)

[31] K. Robbie and M. Brett, "Sculptured thin films and glancing angle deposition: Growth mechanics and applications," *Journal of Vacuum Science & Technology A-Vacuum Surfaces and Films* **15**, 1460–1465 (1997). (Cited on page 7.)

[32] K. Robbie and M. Brett, "US Patent 5 886 204," (1999). (Cited on page 7.)

[33] M. Summers, *Periodic thin films by glancing angle deposition*, PhD thesis, University of Alberta (2009). (Cited on page 10.)

[34] K. Robbie, J. C. Sit, and M. J. Brett, "Advanced techniques for glancing angle deposition," *Journal of Vacuum Science & Technology B: Microelectronics and Nanometer Structures* **16**, 1115–1122 (1998). (Cited on page 10.)

[35] J. B. Sorge, M. A. Summers, M. D. Fleischauer, K. Tabunshchyk, A. Kovalenko, and M. J. Brett, "Ion beam assisted silicon square spiral photonic crystal fabrication," in [*Three-Dimensional Nano- and Microphotonics*], P. Braun, S. Fan, A. Turberfield, and S.-Y. Lin, eds., *Materials Research Society Symposium Proceedings* **1014E**, 1014–AA07–26 (2007). (Cited on pages 10 and 23.)

[36] I. Hodgkinson and Q. H. Wu, "Serial bideposition of anisotropic thin films with enhanced linear birefringence," *Applied Optics* **38**, 3621–3625 (1999). (Cited on page 11.)

[37] A. C. van Popta, J. Cheng, J. C. Sit, and M. J. Brett, "Birefringence enhancement in annealed TiO2 thin films," *Journal of Applied Physics* **102** (2007). (Cited on page 11.)

[38] K. D. Harris, A. C. van Popta, J. C. Sit, D. J. Broer, and M. J. Brett, "A birefringent and transparent electrical conductor," *Advanced Functional Materials* **18**, 2147–2153 (2008). (Cited on page 11.)

[39] A. C. van Popta, J. C. Sit, and M. J. Brett, "Optical properties of porous helical thin films and the effects of post-deposition annealing," in [*Proceedings of SPIE Volume: 5464 - Organic Optoelectronics and Photonics*], 198–208 (2004). (Cited on page 11.)

[40] M. M. Hawkeye and M. J. Brett, "Narrow bandpass optical filters fabricated with one-dimensionally periodic inhomogeneous thin films," *Journal of Applied Physics* **100** (2006). (Cited on page 11.)

[41] S. Kennedy and M. Brett, "Porous broadband antireflection coating by glancing angle deposition," *Applied Optics* **42**, 4573–4579 (2003). (Cited on page 11.)

[42] A. van Popta, J. Sit, and M. Brett, "Optical properties of porous helical thin films," *Applied Optics* **43**, 3632–3639 (2004). (Cited on page 11.)

[43] M. Jensen and M. Brett, "Square spiral 3D photonic bandgap crystals at telecommunications frequencies," *Optics Express* **13**, 3348–3354 (2005). (Cited on pages 11, 14, and 23.)

[44] M. A. Summers and M. J. Brett, "Optimization of periodic column growth in glancing angle deposition for photonic crystal fabrication," *Nanotechnology* **19** (2008). (Cited on page 11.)

[45] M. A. Summers, K. Tabunshchyk, A. Kovalenko, and M. J. Brett, "Fabrication of 2D-3D photonic crystal heterostructures by glancing angle deposition," *Photonics and Nanostructures-Fundamentals and Applications* **7**, 76–84 (2009). (Cited on page 11.)

[46] K. Harris, J. McBride, K. Nietering, and M. Brett, "Fabrication of porous platinum thin films for hydrocarbon sensor applications," *Sensors and Materials* **13**, 225–234 (2001). (Cited on page 11.)

[47] M. Suzuki, T. Ito, and Y. Taga, "Photocatalysis of sculptured thin films of TiO2," *Applied Physics Letters* **78**, 3968–3970 (2001). (Cited on page 11.)

[48] G. Kiema, M. Colgan, and M. Brett, "Dye sensitized solar cells incorporating obliquely deposited titanium oxide layers," *Solar Energy Materials and Solar Cells* **85**, 321–331 (2005). (Cited on page 11.)

[49] K. D. Harris, J. C. Sit, and M. J. Brett, "Fabrication and optical characterization of template-constructed thin films with chiral nanostructure," *IEEE Transactions on Nanotechnology* **1**, 122–128 (2002). (Cited on page 11.)

[50] J. Steele, J. Gospodyn, J. Sit, and M. Brett, "Impact of morphology on high-speed humidity sensor performance," *IEEE Sensors Journal* **6**, 24–27 (2006). (Cited on page 11.)

[51] J. J. Steele, A. C. van Popta, M. M. Hawkeye, J. C. Sit, and M. J. Brett, "Nanostructured gradient index optical filter for high-speed humidity sensing," *Sensors and Actuators B-Chemical* **120**, 213–219 (2006). (Cited on page 11.)

[52] M. Seto, K. Robbie, D. Vick, M. Brett, and L. Kuhn, "Mechanical response of thin films with helical microstructures," *Journal of Vacuum Science & Technology B* **17**, 2172–2177 (1999). (Cited on page 11.)

[53] M. W. Seto, B. Dick, and M. J. Brett, "Microsprings and microcantilevers: Studies of mechanical response," *Journal of Micromechanics and Microengineering* **11**, 582–588 (2001). (Cited on page 11.)

[54] G. Zhang and Y. Zhao, "Mechanical characteristics of nanoscale springs," *Journal of Applied Physics* **95**, 267–271 (2004). (Cited on page 11.)

[55] S. Fernando, A. Elias, and M. Brett, "Mechanical properties of helically perforated thin films," *Journal of Materials Research* **21**, 1101–1105 (2006). (Cited on page 11.)

[56] S. Kesapragada, P. Victor, O. Nalamasu, and D. Gall, "Nanospring pressure sensors grown by glancing angle doposition," *Nano Letters* **6**, 854–857 (2006). (Cited on page 11.)

[57] A. Elias, K. Harris, C. Bastiaansen, D. Broer, and M. Brett, "Large-area microfabrication of three-dimensional, helical polymer structures," *Journal of Micromechanics and Microengineering* **15**, 49–54 (2005). (Cited on page 11.)

[58] P. Hrudey, K. Westra, and M. Brett, "Highly ordered organic Alq3 chiral luminescent thin films fabricated by glancing-angle deposition," *Advanced Materials* **18**, 224+ (2006). (Cited on page 11.)

[59] P. C. P. Hrudey, B. Szeto, and M. J. Brett, "Strong circular Bragg phenomena in self-ordered porous helical nanorod arrays of Alq(3)," *Applied Physics Letters* **88** (2006). (Cited on page 11.)

[60] D. A. Gish, M. A. Summers, and M. J. Brett, "Morphology of periodic nanostructures for photonic crystals grown by glancing angle deposition," *Photonics and Nanostructures - Fundamentals and Applications* **4**, 23–29 (2006). (Cited on page 12.)

[61] J. Nieuwenhuizen and H. Haanstra, "Microfractography of thin films," *Philips Technical Review* **27**, 87–91 (1966). (Cited on page 12.)

[62] H. Vankranenburg and C. Lodder, "Tailoring growth and local composition by oblique-incidence deposition - a review and new experimental-data," *Materials Science & Engineering R-Reports* **11**, 295–354 (1994). (Cited on page 12.)

[63] D. Vick, T. Smy, and M. Brett, "Growth behavior of evaporated porous thin films," *Journal of Materials Research* **17**, 2904–2911 (2002). (Cited on page 12.)

[64] O. Toader and S. John, "Square spiral photonic crystals: Robust architecture for microfabrication of materials with large three-dimensional photonic band gaps," *Physical Review E* **66** (2002). (Cited on pages 12, 14, and 23.)

[65] M. Jensen and M. Brett, "Porosity engineering in glancing angle deposition thin films," *Applied Physics A-Materials Science & Processing* **80**, 763–768 (2005). (Cited on pages 12, 13, 14, and 47.)

[66] D. Ye, T. Karabacak, R. Picu, G. Wang, and T. Lu, "Uniform Si nanostructures grown by oblique angle deposition with substrate swing rotation," *Nanotechnology* **16**, 1717–1723 (2005). (Cited on pages 15 and 23.)

[67] M. D. Fleischauer, J. B. Sorge, R. A. Joseph, and M. J. Brett, "Enhanced control of porous thin film morphology via ion bombardment," in [*Self Assembly of Nanostructures Aided by Ion- or Photon-Beam Irradiation—Fundamentals and Applications*], R. Kalyanaraman, U. Valbusa, and Z. Zhang, eds., *Materials Research Society Symposium Proceedings* **960E**, 0960–N01–03 (2007). (Cited on page 23.)

[68] G. Kalyuzhny, A. Vaskevich, G. Ashkenasy, A. Shanzer, and I. Rubinstein, "UV/vis spectroscopy of metalloporphyrin and metallophthalocyanine monolayers self-assembled on ultrathin gold films," *Journal of Physical Chemistry B* **104**, 8238–8244 (2000). (Cited on pages 27 and 57.)

[69] G. Kalyuzhny, M. Schneeweiss, A. Shanzer, A. Vaskevich, and I. Rubinstein, "Differential plasmon spectroscopy as a tool for monitoring molecular binding to ultrathin gold films," *Journal of the American Chemical Society* **123**, 3177–3178 (2001). (Cited on pages 27 and 57.)

[70] M. Malinsky, K. Kelly, G. Schatz, and R. Van Duyne, "Chain length dependence and sensing capabilities of the localized surface plasmon resonance of silver nanoparticles chemically modified with alkanethiol self-assembled monolayers," *Journal of the American Chemical Society* **123**, 1471–1482 (2001). (Cited on pages 27 and 59.)

[71] A. Haes and R. Van Duyne, "A nanoscale optical blosensor: Sensitivity and selectivity of an approach based on the localized surface plasmon resonance spectroscopy of triangular silver nanoparticles," *Journal of the American Chemical Society* **124**, 10596–10604 (2002). (Cited on page 27.)

[72] M. Lahav, A. Vaskevich, and I. Rubinstein, "Biological sensing using transmission surface plasmon resonance spectroscopy," *Langmuir* **20**, 7365–7367 (2004). (Cited on pages 27 and 57.)

[73] S. Chaney, S. Shanmukh, R. Dluhy, and Y. Zhao, "Aligned silver nanorod arrays produce high sensitivity surface-enhanced Raman spectroscopy substrates," *Applied Physics Letters* **87** (2005). (Cited on pages 27 and 57.)

[74] I. Doron-Mor, H. Cohen, Z. Barkay, A. Shanzer, A. Vaskevich, and I. Rubinstein, "Sensitivity of transmission surface plasmon resonance (T-SPR) spectroscopy: Self-assembled multilayers on evaporated gold island films," *Chemistry-A European Journal* **11**, 5555–5562 (2005). (Cited on pages 27 and 57.)

[75] H. Park, J. Yoon, and K. Kim, "Novel fabrication of Ag thin film on glass for efficient surface-enhanced Raman scattering," *Langmuir* **22**, 1626–1629 (2006). (Cited on page 27.)

[76] Y. Yang, L. Xiong, J. Shi, and M. Nogami, "Aligned silver nanorod arrays for surface-enhanced Raman scattering," *Nanotechnology* **17**, 2670–2674 (2006). (Cited on page 27.)

[77] T. Arai, P. Kumar, K. Awazu, and J. Tominaga, "Localized Surface Plasmon Resonance Biosensor Using Ag Nanostructured Films Fabricated by a Reduction Method," in [*Nanostructured Materials and Hybrid Composites for Gas Sensors and Biomedical Applications*], **915**, 0915–R02–08 (2006). (Cited on pages 27 and 59.)

[78] I. Tanahashi, F. Yamazaki, and K. Hamada, "Localized surface plasmon resonance sensing properties of Ag/TiO2 films," *Chemistry Letters* **35**, 454–455 (2006). (Cited on pages 27 and 59.)

[79] S. Malynych and G. Chumanov, "Coupled planar silver nanoparticle arrays as refractive index sensors," *Journal of Optics A-Pure and Applied Optics* **8**, S144–S147 (2006). (Cited on pages 27 and 59.)

[80] Y. Zhao, S. Chaney, S. Shanmukh, and R. Dluhy, "Polarized surface enhanced raman and absorbance spectra of aligned silver nanorod arrays," *Journal of Physical Chemistry B* **110**, 3153–3157 (2006). (Cited on pages 27 and 57.)

[81] M. Suzuki, W. Maekita, Y. Wada, K. Nakajima, K. Kimura, T. Fukuoka, and Y. Mori, "In-line aligned and bottom-up Ag nanorods for surface-enhanced Raman spectroscopy," *Applied Physics Letters* **88** (2006). (Cited on pages 27 and 57.)

[82] U. Kreibig and M. Vollmer, *Optical Properties of Metal Clusters*, Springer-Verlag: Berlin (1995). (Cited on page 27.)

[83] K. A. Willets and R. P. Van Duyne, "Localized surface plasmon resonance spectroscopy and sensing," *Annual Review of Physical Chemistry* **58**, 267–297 (2007). (Cited on pages 27 and 28.)

[84] J. Sambles, G. Bradbery, and Y. Fuzi, "Optical excitation of surface plasmons: an introduction.," *Contemporary Physics* **32**, 173 (1991). (Cited on page 27.)

[85] G. Mie, "Articles on the optical characteristics of turbid tubes, especially colloidal metal solutions.," *Annalen der Physik* **25**, 377–445 (1908). (Cited on page 28.)

[86] A. Haes and R. Van Duyne, "A unified view of propagating and localized surface plasmon resonance biosensors," *Analytical and Bioanalytical Chemistry* **379**, 920–930 (2004). (Cited on page 28.)

[87] E. Zeman and G. Schatz, "An accurate electromagnetic theory study of surface enhancement factors for Ag, Au, Cu, Li, Na, Al, Ga, In, Zn, and Cd," *Journal of Physical Chemistry* **91**, 634–643 (1987). (Cited on pages 28 and 29.)

[88] T. A. Bendikov, A. Rabinkov, T. Karakouz, A. Vaskevich, and I. Rubinstein, "Biological sensing and interface design in gold island film based localized plasmon transducers," *Analytical Chemistry* **80**, 7487–7498 (2008). (Cited on page 32.)

[89] S. Haemers, G. Koper, M. van der Leeden, and G. Frens, "An alternative method to quantify surface plasmon resonance measurements of adsorption on flat surfaces," *Langmuir* **18**, 2069–2074 (2002). (Cited on page 32.)

[90] A. Kumbhar, M. Kinnan, and G. Chumanov, "Multipole plasmon resonances of submicron silver particles," *Journal of the American Chemical Society* **127**, 12444–12445 (2005). (Cited on pages 33 and 36.)

[91] K. Kelly, E. Coronado, L. Zhao, and G. Schatz, "The optical properties of metal nanoparticles: The influence of size, shape, and dielectric environment," *Journal of Physical Chemistry B* **107**, 668–677 (2003). (Cited on page 36.)

[92] M. Mcmahon, R. Lopez, H. Meyer, L. Feldman, and R. Haglund, "Rapid tarnishing of silver nanoparticles in ambient laboratory air," *Applied Physics B-Lasers and Optics* **80**, 915–921 (2005). (Cited on page 50.)

[93] D. A. Gish, F. Nsiah, M. T. McDermott, and M. J. Brett, "Localized surface plasmon resonance biosensor using silver nanostructures fabricated by glancing angle deposition," *Analytical Chemistry* **79**, 4228–4232 (2007). (Cited on page 53.)

[94] V. Kanda, J. Kariuki, D. Harrison, and M. McDermott, "Label-free reading of microarray-based immunoassays with surface plasmon resonance imaging," *Analytical Chemistry* **76**, 7257–7262 (2004). (Cited on pages 53 and 62.)

[95] R. Van Duyne, J. Hulteen, and D. Treichel, "Atomic-force microscopy and surface-enhanced Raman-spectroscopy. 1. Ag island films and Ag film over polymer nanosphere surfaces supported on glass," *Journal of Chemical Physics* **99**, 2101–2115 (1993). (Cited on page 57.)

[96] G. Xu, M. Tazawa, P. Jin, and S. Nakao, "Surface plasmon resonance of sputtered Ag films: substrate and mass thickness dependence," *Applied Physics A-Materials Science & Processing* **80**, 1535–1540 (2005). (Cited on page 57.)

[97] J. Martinez, Y. Gao, and T. Lopezrios, "Surface-enhanced raman-scattering of obliquely evaporated Ag films," *Physical Review B* **33**, 5917–5919 (1986). (Cited on page 57.)

[98] J. Martinez, Y. Gao, T. Lopezrios, and A. Wirgin, "Anisotropic surface-enhanced Raman-scattering at obliquely evaporated Ag films," *Physical Review B* **35**, 9481–9488 (1987). (Cited on page 57.)

[99] M. Suzuki, W. Maekita, K. Kishimoto, S. Teramura, K. Nakajima, K. Kimura, and Y. Taga, "Direct formation of arrays of prolate Ag nanoparticles by dynamic oblique deposition," *Japanese Journal of Applied Physics Part 2-Letters & Express Letters* **44**, L193–L195 (2005). (Cited on page 57.)

[100] R. Brun and F. Rademakers, "ROOT - An object oriented data analysis framework," *Nuclear Instruments & Methods in Physics Research Section A-Accelerators Spectrometers Detectors and Associated Equipment* **389**, 81–86 (1997). (Cited on page 62.)